Cold Air Outbreaks in Midlatitude Asia With and Without Precursory Pulse in the Stratospheric Poleward Warm Air Transport

Zhiqiang Ding[1, 3], Yueyue Yu[1, 3*], Haishan Chen[2, 3],

Xiaocen Shen[4], Ming Cai[5], Yang Liu[1, 3]

[1] *State Key Laboratory of Environment Characteristics and Effects for Near-space, Nanjing 210044, China*

[2] *State Key Laboratory of Climate System Prediction and Risk Management, Nanjing 210044, China*

[3] *Ministry of Education/Collaborative Innovation Center on Forecast and Evaluation of Meteorological Disasters, Nanjing University of Information Science and Technology, Nanjing 210044, China*

[4] *Department of Meteorology, University of Reading, Reading, UK*

[5] *Department of Earth, Ocean Atmospheric Sciences, Florida State University, Tallahassee, FL 32304, USA*

Submitted to Climate Dynamics on March 3, 2026

*Corresponding author address: Yueyue Yu, School of Atmospheric Sciences, Nanjing University of Information Science and Technology, 219 Ning Liu Road, Nanjing 210044, China. E-mail: yuyy@nuist.edu.cn

Abstract

Using ERA5 data from 1979 to 2024, this study classifies 173 wintertime Cold Air Outbreak (CAO) events in midlatitude Asia, based on their temporal phasing relative to pulse-like intensifications of warm air mass transport into the polar stratosphere above 400 K (PULSEs). Two PULSE-related types are identified: PULSE-lead (18.0%), where the PULSE precedes the CAO peak, and PULSE-lag (21.4%), where it follows. PULSE_lead events exhibit slightly more persistent and widespread cold anomalies across Eurasia. The phasing is found to be governed by the planetary-wave driven coupling between the poleward stratospheric warm branch and equatorward tropospheric cold branch of the isentropic meridional mass circulation at 60°N, respectively dominated by warm air transport over the Northwestern Pacific and cold air transport over Asia. PULSE_lead events are preceded by rapid propagation of wavenumber-2 energy into the stratosphere, simultaneously intensify both branches. In contrast, PULSE-lag events are triggered by a stronger Ural ridge and downstream energy dispersion, with delayed wavenumber-1-dominated upward wave flux strengthening the stratospheric warm branch only after the CAO. While PULSE_lag events are mainly caused by tropospheric processes, a downward impact from the stratosphere is found for PULSE_lead. The precursory PULSE induces a stratospheric mass deficit over the East Asian trough region, resulting in barotropic low anomalies, which helping maintain the trough and prolong the CAO. Furthermore, PULSE_lead events have detectable stratospheric polar vortex anomalies 2 weeks in advance. This study clarifies the diversity of CAO formation mechanisms and demonstrates the existence of a subset involving active stratospheric pulse-like precursors.

Key Words: Cold air outbreak; Isentropic meridional mass circulation; Stratosphere-troposphere coupling; Stratospheric polar vortex

1 Introduction

Cold Air Outbreak (CAO) events in Asia represents southward intrusion of polar air masses, inducing widespread cold temperatures across mid-latitudes. The convergence of this cold air with warm moist air from the south often causes hazardous weather, including heavy snowfall, freezing rain, and strong winds, imposing substantial socioeconomic risks (Shi et al. 2020; Deng and Xu 2024). Asian CAOs occurred 8~10 times per winter (Chen et al. 2004; Yu et al. 2018a) and a pronounced warm Arctic–cold Eurasia trend pattern has been observed from the early 1990s to the early 2010s, even under global warming (Francis and Vavrus 2012; Cohen et al. 2014; Francis et al. 2017). Therefore, improving prediction skills of Asian CAOs remains a major priority for operational forecasting centers.

Asian CAOs are primarily driven by tropospheric circulation anomalies. Synoptic systems such as the Siberian High and Mongolian cyclones are often coupled with the Ural blocking high and deepened East Asian trough above, which govern the near-surface cold air accumulation and advection (Cohen et al. 2001; Cheung et al. 2012; Miao and Wang 2020; Hwang et al. 2022; Cholaw et al. 2022; Zhang and Lu 2022, Dong et al. 2023; Li et al. 2024). Meridional and zonal teleconnection patterns also play an important role. The negative phase of the Arctic Oscillation (AO) establishes the large-scale circulation background that facilitates the southward advance of cold air masses (Park and Ahn, 2016; Gong et al., 2019, 2022, 2024). The multidecadal fluctuations of the AO dominates Eurasian winter surface air temperature trends and CAO occurrence on interannual to interdecadal timescales, with dynamical processes contributing over 60%–80% of the total variance and even higher (~85%) to for extreme cold events. Meanwhile, the negative phase of the Eurasian (EU) pattern provides direct forcing for the intensification and persistence of the East Asian trough and the Ural High by establishing a canonical “western ridge-eastern trough” anomaly pattern (Wu and Wang 2002; Lim and Kim 2013; Liu et al. 2014; Maeda et al. 2021). Beside these

internal variabilities, Arctic amplification (AA)-related forcing (e.g., Barents-Kara Sea sea-ice loss) can accumulate through persistent positive feedbacks on multidecadal scales, contributing approximately -0.24 K/decade to central Eurasian cooling and effectively suppressing externally forced warming to form a "warming hole" since 1980 (Gong et al., 2025). A closer investigation on individual events yields two distinct types of Asian CAOs (Park et al. 2014, 2015): i) Wave-train type, driven by baroclinic wave trains (positive in west Siberia, negative in Northeast China, positive in Northwestern Pacific), similar to the negative EU pattern and ii) Blocking type, tied to a height dipole consisting of the subarctic blocking and the East Asian coastal trough to the south, accompanied by a negative AO. However, these tropospheric signals exhibit limited predictability beyond two weeks (Simmons and Hollingsworth 2002; Zhang et al. 2019), while tropical predictability sources such as the El Niño-Southern Oscillation (ENSO) and Madden-Julian Oscillation (MJO) provide predictive skills during specific phases only (Dasgupta et al. 2021; Mayer et al. 2024). Exploring new predictability source is still in need.

Growing attention has been drawn to the neighbor above the extratropical troposphere, which is the stratospheric polar vortex (SPV), because of its higher predictability beyond 2 weeks by current operational models (Tripathi et al. 2015; Domeisen et al. 2020), lower-frequency variability (Cai and Ren 2007; Yu et al. 2018b), and downward impact (e.g., Baldwin et al. 2001). Particularly, 1-2 months after a weaker SPV or a stratospheric sudden warming (SSW) event, cold anomalies are more likely to occur over Eurasian and North American continents (Thompson et al. 2002; Kidston et al. 2015; Lehtonen and Karpechko 2016). Zhang et al. (2025) objectively classified Asian CAO events into three types (south, mixed, and north) based on the locations of core cold anomalies, and found that they are accompanied by different strength of pre-existing stratospheric polar vortex, a background under which even similar wave activities can result in dissimilar upper-tropospheric circulation anomalies over East Asia leading to different extents and magnitudes of anomalous coldness. The pulse-like intensification of stratospheric poleward warm air mass transport or heat flux into the polar stratosphere (denoted as "PULSE" in Cai et al. 2016) exhibits a quasi-

biweekly periodicity, which dynamically dominates the weakening of SPV (Polvani and Waugh 2004; Yu et al. 2018a, b, c; Dunn-Sigouin and Shaw 2020). Within the framework of the isentropic meridional mass circulation (Johnson 1989; Cai and Shin 2014), these PULSE events are often coupled with strengthened equatorward transports of polar cold air in the lower troposphere, both driven by westward-tilted, deep-structured planetary waves (Yu et al. 2015a, b; Yu and Ren 2019). The frequently occurring PULSE events are argued to be more effective stratospheric indicators of individual CAO events than rare SSWs and the slow-varying SPV intensity (Yu et al. 2018a). In addition, PULSE can provide forecasts 20 days in advance by operational models like Climate Forecast System Version 2 (CFSv2) (Cai et al. 2016; Yu et al. 2019; Domeisen et al. 2020), thus serving as a sub-seasonal forecasting candidate for CAO.

However, utilizing stratospheric signals in forecasting CAOs in Asia is a particular challenge because Asian CAOs often precede both weak SPV events and pulse-like stratospheric disturbances. This suggests that the circulation anomalies and large-scale waves associated with Asian CAOs appear to be a cause rather than a consequence of stratospheric anomalies. Many studies (Kolstad et al. 2010; Woo et al. 2015; Yu et al. 2024) consistently conclude that Asian cooling is more commonly seen during the two weeks before the central dates of SSWs, the peak dates of weaker SPV events and PULSE events. This pre-event cooling is particularly pronounced during wave-1-dominated processes (Yu et al. 2018a; Zhou et al. 2024; Choi et al. 2021). Nevertheless, counterexamples exist. During the 2020/21 winter, Asia experienced two successive record-breaking CAOs, with the second following SSW and PULSE events (Yu et al. 2021; Zhang et al. 2022; Davis et al. 2022). Moreover, CAOs with stratospheric precursors tend to be exceptionally severe and long-lasting (Park et al. 2014; Garfinkel et al. 2017; Zhang et al. 2022; Huang et al. 2025). Although Asian CAOs with stratospheric precursors are not the majority, they deserve particular attention, as they represent window of opportunity for utilizing stratospheric signals in the sub-seasonal forecasts.

To distinguish between Asian CAOs with and without precursory PULSE signals, we developed an objective classification framework based on a lagged time-domain

Empirical Orthogonal Function (EOF) analysis of stratospheric poleward warm air mass transport. Using such classification, we then investigated the characteristics of these two types, explored the associated circulation patterns, wave activity and propagation, and isentropic air mass distribution as key processes in stratosphere-troposphere coupling. Our particular focus is on two questions: (i) What mechanisms allow PULSEs to precede certain Asian CAO events? (ii) Through what pathways do these precursory PULSE events exert downward influence to amplify subsequent CAOs?

2 Data and Methods

2.1 Data

The data used include daily mean 2-m temperature (T_{2m}), surface pressure (Ps), three-dimensional geopotential (z), air temperature (T), meridional wind (v), and zonal wind (u) fields derived from the 6-hour daily ERA5 data from November 1979 to March 2025 (Hersbach et al., 2020). The data fields are on 1.5° × 1.5° grids and 37 levels from 1000 to 1 hPa. Surface and three-dimensional potential temperature fields (θ_s and θ) were calculated from the Ps, T_{2m} and T. T-N wave activity fluxes were derived from daily fields of z, T, u, v (Takaya and Nakamura 2001). Thermodynamic tropopause pressure data is from the National Centers for Environmental Prediction.

A winter is defined as the period from November 1 of one year to March 31 of the next. Daily climatological mean fields were obtained by first calculating the multi-year (1979–2024) average for each calendar day from November 1 to March 31, and then applying a 31-day running mean. Anomaly fields were derived by subtracting the climatological mean of the corresponding calendar day from the raw data. The winter mean for each year was removed to filter out interannual variability modulated by external forcing, such as ENSO. A 7-day filtering was further applied to suppress high-frequency synoptic noise.

2.2 Calculation scheme of isentropic layer mass and meridional mass flux

Following the approaches of Yu et al. (2014, 2015b), the isentropic layer mass and meridional mass flux were computed across 16 layers. Fifteen specific isentropic levels were selected: Θ_n(n=1, 15)=250, 260, 270, 280, 290, 300, 315, 330, 350, 370, 400, 450, 550, 650, and 850 K. These define 14 adjacent isentropic layers, with values specified at the lower surface of each layer. An additional lowest layer (denoted as "<250 K") and a top layer (denoted as ">850 K") were included to complete the 16-layer structure using potential temperature as the vertical coordinate. *v* and θ fields are interpolated onto 200 equally spaced iso-sigma surfaces (σ-levels) ranging from 0 to 1. Values below θ_s are considered as below ground, thus removed. Based on whether the potential temperature of an air parcel falls within the range of Θ_n to Θ_{n+1}, the mass and meridional mass flux in each isentropic layer are obtained:

$$mv_\theta(\lambda,\phi,\Theta_n,t)=\int_0^1 P_s(\lambda,\phi,t)\frac{\delta\sigma}{g}\cdot v(\lambda,\phi,\sigma,t)\cdot Y(\theta(\lambda,\phi,\sigma,t),\Theta_n,\Theta_{n+1})d\sigma, \quad (1)$$

$$m_\theta(\lambda,\phi,\Theta_n,t)=\int_0^1 P_s(\lambda,\phi,t)\frac{\delta\sigma}{g}\cdot Y(\theta(\lambda,\phi,\sigma,t),\Theta_n,\Theta_{n+1})d\sigma, \quad (2)$$

where ϕ denotes latitude, λ denotes longitude, and t denotes time. δσ=1/200, g is the gravitational acceleration (9.8 m/s^2), and *Y(x, x_1, x_2)* is a boxcar function that equals 1 when $x_1 \le x < x_2$ and 0 otherwise. Equations (1) and (2) were applied for layers Θ_n (where n = 1 to 14). For the lowest layer (n = 0), Θ_n was replaced by 0, and for the top layer (n = 15), Θ_{n+1} was replaced by +∞. A positive (negative) value of mv_θ corresponds to northward (southward) transport of air mass with specific thermal characteristics.

The zonal integrals of mv_θ and m_θ are as follows. The integration of mass or mass flux over the specified longitudinal range yields the following.

$$\mathrm{MV}_\theta(\phi,\Theta_n,t)=\int_{\lambda_1}^{\lambda_2}\int_0^1 P_s(\lambda,\phi,t)\frac{\delta\sigma}{g}\cdot v(\lambda,\phi,\sigma,t)\cdot Y(\theta(\lambda,\phi,\sigma,t),\Theta_n,\Theta_{n+1})d\sigma\, d\lambda, \quad (3)$$

$$\mathrm{M}_\theta(\phi,\Theta_n,t)=\int_{\lambda_1}^{\lambda_2}\int_0^1 P_s(\lambda,\phi,t)\frac{\delta\sigma}{g}\cdot Y(\theta(\lambda,\phi,\sigma,t),\Theta_n,\Theta_{n+1})d\sigma d\lambda, \quad (4)$$

λ_1 and λ_2 denote the outer boundaries of the required longitudinal integration range.

In the winter hemisphere, $mv_\theta>0$ in the upper troposphere and stratosphere but <0 in the lower troposphere, forming a hemispheric meridional mass circulation characterized by poleward transport of warm air (denoted as the "warm branch") and equatorward transport of cold air (denoted as the "cold branch"), consistent with Cai and Shin (2014).

To quantify the intensity of stratospheric poleward warm air transport, we follow Cai et al. (2016) and define an ST60N index, which is the net poleward transport of warm air mass above the 400K in unit of kg per second.

$$ST60N(t) = \int_0^{2\pi} \sum_{\Theta_n=400K}^{>850K} mv_\theta(\lambda, \phi = 60°N, \Theta_n, t)\, Rcos\phi d\lambda, \quad (5)$$

where R is the Earth's radius. Thereafter, the ST60N index was standardized.

The wavenumber-1 and -2 components of the mv_θ and ST60N (denoted as ST60N_W1 and ST60N_W2) are derived by decomposing v into its spectral components (v_1 and v_2) using Fourier transform, which are then substituted for v in Equations (1) and (3).

2.3 Asian cold area index and selection of CAO events

This study employs the cold area percentage (CAP) index defined by Cai (2003) and Yu et al. (2015a), which quantifies the percentage of grid points within a specific region where the T_{2m} anomaly falls below -0.5 times the local standard deviation (LSD) across all winter days. The region used in this study spans over Asia (30°–60°N and 60°–135°E), denoted as Asian CAP (ACAP). The threshold of -0.5 LSD was selected because it captures moderate yet statistically significant cold anomalies, providing a balanced criterion for identifying coherent and meteorologically relevant CAOs across the extensive and topographically diverse study region.

An Asian CAO event is identified when the ACAP index exceeds the 50th percentile (26.4 %) for at least two consecutive days, with its peak surpassing the 70th percentile (37.4 %). The 50th percentile threshold ensures that the cold coverage exceeds the winter median, while the peak threshold has also been tested using the 65th and 75th percentiles, and the main results remain qualitatively unchanged. The period of the

event is defined by the start and end dates during which the index remains above the 50th percentile. We require that two adjacent events must be separated by at least three days, otherwise only the event exhibiting the higher maximum value is retained. The peak date corresponds to the day with the maximum value during the event's duration. A total of 173 CAO events were identified during winters from 1979 to 2024.

3 Temporal Phasing between Stratospheric Poleward Warm Air Transport Anomalies and Asian CAOs

3.1 Temporal Phasing-based Classification of CAO

The spectrum of both ACAP and ST60N indices shows pronounced peaks at quasi-biweekly timescales (Fig. 1), confirming a close temporal alignment between Asian CAO and PULSE events, as indicated by Yu et al. (2018c). The composite evolution of ST60N shows statistically significant and persistent positive values during and after the peak dates of CAO (Fig. 2a), consistent with PULSEs often emerging after Asian CAOs (Woo et al. 2015; Yu et al. 2024). After decomposing ST60N into different wavenumbers, the wavenumber-1 component shows a clear increase with time and peaks around day +7, contributing to the peak of ST60N after CAO peak. This phase relationship supports the established finding that in events dominated by strong wavenumber-1 waves, such as displacement-type SSWs and wavenumber-1-dominant PULSE events, Eurasian cold events typically peak before the central stratospheric signal (e.g., Hyesun et al. 2021; Zhou et al. 2024). In contrast, the ST60N_W2 peaks almost concurrently with the ACAP index, aligning with previous reports that Asian CAOs tend to occur concurrently with split-type SSWs and wavenumber-2-dominant PULSE events (Kuttippurath and Nikulin 2012; Yu et al. 2018c).

However, an event-by-event examination reveals that not all Asian CAOs lack a precursory stratospheric PULSE signal. To objectively classify their temporal phasing relationships, EOF analysis was applied to the 173 temporal evolutions of the ST60N

index, centered on the peak dates of CAO events (±7 days). The evolution from Day -7 to Day +7 is considered as the "spatial" dimension and the number of CAO events is the "temporal" dimension. The two dominant resulting modes are shown in Fig. 3. The positive phase of the leading mode (EOF1, 30.0% variance) exhibits strongly positive ST60N values in the week preceding the CAO peak, suggesting the presence of a precursory stratospheric pulse signal. Conversely, the positive phase of the second mode (EOF2, 28.2% variance) features PULSEs in the week following the CAO peak. Based on the ST60N evolution patterns, CAO events were further classified into two distinct categories coupled with PULSEs. Events were classified as PULSE_lead if the principal component of the EOF1 (PC1) exceeded +0.5σ, and EOF1 dominated the event' s evolution, with the absolute value of PC1 being greater than that of PC2. Conversely, events satisfying these same criteria for the EOF2 mode were categorized as PULSE_lag, indicating cases where the stratospheric PULSE follows the CAO peak.

This classification framework identified 31 PULSE_lead events and 37 PULSE_lag events, respectively accounting for 18.0% and 21.4% of the total, highlighting the different roles of stratospheric precursors versus subsequent feedbacks in the evolution of CAOs in Asia. The composite evolution of the ST60N index differs markedly between the two types, demonstrating that the validity and effectiveness of the classification method.

3.2 Different Characteristics of Cold Extremes in Two Types of CAO

Figs. 2b and 2c display the composite ACAP index evolution during the ±7-day windows centered on the peak dates of the PULSE_lead and PULSE_lag CAO events, with the significance of the composite was determined using a two-sample t-test at the 95% confidence level by comparing event samples with all winter samples, ensuring high consistency of anomalies among individual events within each category. A comparison between two types of events reveals two features. The peak magnitudes of composite mean ACAP index are comparable (~60%), indicating no detectable difference in the maximum cold area coverage. However, PULSE_lead events tend to

maintain statistically significant values of ACAP for approximately one day longer on average than PULSE_lag events, with a difference observed on the fourth day after the peak. Fig. 4 further shows the spatial distribution of the occurrence probability of cold extremes, defined as T_{2m} anomalies below -0.5 LSD (medium-to-intense) and -1 LSD (intense), averaged over the duration of the CAO events of each type. It is seen that during both types, a "warm Arctic – cold midlatitude continent" pattern dominates the Eurasian sector, with fewer occurrence probabilities of cold extremes over the high-latitude Western Russia/Siberian Arctic but more over Central and East Asia. In Mongolia and northern/eastern China, the probability of medium-to-intense cold anomalies exceeds 50%, which is 30% higher than the winter climatology, while intense cold anomalies surpass 35% (20% above climatology). The key difference between two types of CAOs is the spatial extent. During PULSE_lead events, elevated cold anomaly probabilities cover nearly the entire midlatitude Eurasian continent. Eastern China in particular experiences a more extensive and continuous area with a $\geqslant$30% probability increase for medium-to-intense cold, compared to PULSE_lag events. In general, PULSE_lead events are characterized by a slightly more persistent, widespread cold anomaly pattern across Eurasia than PULSE_lag events, consistent with the modest difference in the composite mean values of ACAP index between the two types, as shown in Figs 2b and 2c.

3.3 Vertical Profiles of Isentropic Meridional Mass Fluxes

Because the daily variations of isentropic meridional mass circulation around 60°N redistribute cold and warm air masses in the extratropics, dynamically driving the "warm Arctic-cold midlatitudes" pattern (Yu et al. 2015a; Sorokina et al. 2016; Lin et al. 2025), we next examine the longitudinal and vertical structure of isentropic meridional mass fluxes across 60°N ($mv_\theta(\lambda,\phi=60°N,\Theta_n,t)$)and their zonally integral around peak dates of CAOs, in order to demonstrate how PULSE events, i.e., intensified warm air mass transport into the polar stratosphere, are connected to nearly half of CAOs in Asia.

During the week before both PULSE_lead (Figs. 5a) and PULSE_lag (Figs. 6a) events, statistically significant negative anomalies of mv_θ are present within the 60°E–120°E sector, extending from below 250K to 650K. These anomalies below 280K indicate a stronger equatorward transport of cold polar air through the Asian route, which is one of the three main routes of cold air outbreaks identified by Iwasaki et al. (2012) and Yu et al. (2024). Simultaneously, positive anomalies are observed within the 10°E–60°E sector, but the longitudinal extent of this signal below 270 K is notably narrower than that of the equatorward transport. This suggests an intensified poleward mass transport of warmer air to the west of cold air intrusion. Together, this zonal dipole pattern in isentropic mass flux anomalies across the polar circle provides a dynamical explanation for the "warm Arctic–cold midlatitude Eurasia" configuration shown in Fig. 4. This dipole pattern had largely vanished one week after the CAO peaks.

From Figs. 5a and 6a, we can observe a zonal dipole pattern in mv_θ anomalies at stratospheric layers above 330 K. This pattern consists of the previously mentioned negative mv_θ anomalies over Asia extending from the bottom, and positive anomalies to the east over Northwestern Pacific (120°E–150°E), which is the primary and vertically deepest climatological route for warm air transport into the polar stratosphere as indicated by the climatology. However, these positive anomalies observed in the week before PULSE_lag events are much weaker and narrower than those associated with PULSE_lead events (compare Figs. 5a and 6a). Instead, widespread positive anomalies only emerged in the subsequent week of PULSE_lag events (Fig. 6b).

From the isentropic meridional mass circulation perspective or zonal integral perspective (right panels of Figs. 5a and 6a), we find that during the week before both types, the strengthened equatorward mass fluxes via the Asian route were associated with a strengthened cold branch of the isentropic meridional mass circulation, indicated by significantly negative anomalies in the zonally integrated mv_θ between 260–270 K. Coupled with the strengthening of cold branch was the strengthening of the warm branch aloft, but the layers of strengthening differ: in the stratosphere (above 350 K) for PULSE_lead but in the mid-upper troposphere (290–315 K) for PULSE_lag. In addition, we can see the co-occurrence of positive zonally integrated mv_θ anomalies

above 350 K and positive mv_θ anomalies over the Northwestern Pacific region in the week before PULSE_lead events as well as the week after PULSE_lag events, suggesting that poleward warm air transport in this sector often dominates the total stratospheric warm air transport across 60°N. Therefore, due to the regional coupling between equatorward cold air transport over the Asian sector and poleward warm air transport over the Northwestern Pacific sector within the stratosphere, a uniquely deep vertical coupling exists between the cold branch and the stratospheric warm branch of the isentropic meridional mass circulation before PULSE_lead-type Asian CAO events, which has been observed among continental-scale CAOs with precursory PULSEs and higher subseasonal predictability (Yu et al. 2022, 2023; Yang et al. 2025).

Wave decomposition of isentropic meridional mass fluxes further clarifies the roles of planetary waves in the two types of CAO events. Specifically, the composite evolution of ST60N_W1 and ST60N_W2 (Figs. 2b and 2c) shows that PULSE_lead events are primarily driven by enhanced wavenumber-2 activity prior to the event. In contrast, PULSE_lag events arise are contributed from both wavenumbers after the event, with wavenumber-1 dominating. A closer examination of the decomposed mv_θ anomalies at 60°N (Figs. 5c–d and Figs. 6c–6d for wavenumber-1 and Figs. 5e–5f and Figs. 6e–6f wavenumber-2) shows that, for both event types, wavenumber-1 and -2 components of mv_θ anomalies constructively reinforce the climatological phase in the troposphere one week before the event, enhancing cold and warm air exchange between polar and mid-latitude regions and thus the CAO signature. For PULSE_lead events, the wavenumber-2 components extend upward with a slight westward tilt, leading to poleward zonal integrated mv_θ anomalies from 300 K up to 650 K in the prior week, whereas wavenumber-1 shows no significant stratospheric anomaly. For PULSE_lag events, however, constructive superposition of both wavenumber-1 (dominant) and wavenumber-2 anomalies onto the climatological flow occurs in the stratosphere specifically during the week after the CAO peak. This implies a delayed upward propagation of planetary wave energy, amplifying stratospheric mass exchange after the tropospheric exchange. These results imply that a pre-existing enhancement of deep structure wavenumber-2 waves is essential for PULSE_lead CAO events in Asia, while

the gradual upward propagation of planetary waves of both wavenumber-1 and -2 may relate to the PULSE_lag events.

Note that in the remaining 60.6% CAO events, which lack a discernible PULSE signature, the mv_θ anomalies at 60°N driven by wavenumber-1 and -2 are weak and statistically insignificant (not shown). This suggests that smaller-scale waves likely dominate the formation of these particular events. Given that planetary wavenumber-1 and -2 serve as key mediators of stratosphere-troposphere coupling, the absence of pronounced activity in these planetary-scale components explains the lack of a clear stratospheric imprint for this subset of CAOs.

4 Mechanism Underlying the Temporal Phasing of Asian CAO and PULSE

4.1 Circulation Patterns in the Troposphere and Stratosphere and Wave Activities

Next, we selected five stages relative to the peak dates of CAO events: 7 to 5 days before (days -7 to -5), 4 to 2 days before (days -4 to -2), 1 day before to 1 day after (days -1 to 1), 2 to 4 days after (days 2 to 4), and 5 to 7 days after (days 5 to 7). We then examined the composite mean large-scale circulation patterns at the 500 hPa level at each stage, as shown in Fig. 7. Prior to the peak dates of both event types, the Ural Ridge and East Asian Trough are noticeably amplified (Figs. 7a–f), a configuration widely documented to favor southward cold air advection from polar regions (e.g., Woo et al. 2015; Zhou et al. 2024). However, combining the composites of T-N wave activity flux, two key differences emerge. First, the magnitude of the high anomalies over the Ural region preceding PULSE_lead events is only about two-thirds of that before PULSE_lag events, indicating a comparatively weaker Ural Ridge during PULSE_lead events. Second, clear downstream wave energy dispersion is only evident prior to PULSE_lag events. As wave energy propagates downstream, the Ural Ridge, which becomes strongest during days –4 to –2, gradually weakens by days –1 to +1, while

downstream negative anomalies intensify, reflecting a deepening of the East Asian Trough (Figs. 7d, f). In contrast, no such upstream wave energy propagation is evident prior to PULSE_lead events. Nevertheless, in these cases, the anomalously deep East Asian Trough is sustained throughout the prior week and even undergoes secondary intensification while shifting eastward between the day –4 to –2 and day –1 to +1 periods (Figs. 7a, c, e).

From the composited stratospheric circulation patterns at 50 hPa and associated vertical component of T-N wave activity flux at 100 hPa (Fig. 8), we see that for PULSE_lead events, significant negative anomalies are present over the Northern Eurasia as early as days –7 to –5, indicating a preconditioning displacement of one low center of the stratospheric polar vortex toward Eurasia. Pronounced positive vertical T-N wave activity fluxes in these regions suggest early upward propagation of wave energy from the troposphere into the stratosphere (Fig. 8a). These upward wave fluxes peak during days –4 to –2, accompanied by the emergence of northward horizontal wave fluxes east of the low anomalies, indicative of poleward heat transport (Fig. 8c). This aligns with the observed poleward warm air mass flux anomalies over the Northwestern Pacific region (Fig. 5a). By days –1 to +1, sustained poleward heat and mass transport contributes to a meridional dipole anomaly pattern (high north and low south) within this longitudinal sector, with the low anomaly center shifting gradually southward (Fig. 8e). This evolution suggests that, prior to PULSE_lead CAO events, a strengthened Ural Ridge paired with an intensified East Asian Trough triggers cold air southward outbreaks across Asia. Concurrently, associated increased wave energy mainly propagates upward into the stratosphere rapidly, strengthening poleward warm air transport downstream of the pre-existing Northern Eurasian low anomaly. Thus, owing to the largely unimpeded upward wave propagation associated with the Ural Ridge intensification, both the stratospheric warm branch and the tropospheric cold branch of the isentropic meridional mass circulation are amplified almost concurrently, preceding the peak of the CAO events belong to the PULSE_lead type.

Distinctively, PULSE_lag events show no significant stratospheric geopotential height anomalies or upward wave fluxes before the CAO peak (days -7 to -2; Figs. 8d,

f). Pronounced upward and poleward wave fluxes emerge only afterwards, resulting in decrease of height in the midlatitude Asia but increase in the polar region, thus weakening the stratospheric polar vortex. By then, the tropospheric circulation at 500 hPa has already transitioned to a zonal flow pattern featured by low anomalies north of 60°N and high anomalies to the south (Figs. 7h, j), creating a contrast with the stratospheric pattern at 50 hPa. This sequence suggests that for PULSE_lag events, a strengthened Ural High enhances the East Asian Trough via downstream wave energy dispersion, collaboratively triggering the CAO. The associated planetary waves then propagate upward slowly, eventually inducing a delayed stratospheric response. Consequently, the stratospheric PULSE appears to be a lagged consequence rather than a precursor of the CAO in these cases.

The stratosphere-troposphere coupling relationship, in terms of the circulation patterns and wave activities, is more clearly illustrated in the pressure-longitude cross-sections of geopotential height anomalies and T-N wave activity fluxes, averaged over 45−65°N, where both the East Asian Trough anomalies and the stratospheric low anomalies are mainly located. As shown in Figs. 9a and 9c, PULSE_lead events exhibit enhanced upward wave activity fluxes over the Ural high region and its upstream area, which propagate predominantly upward into the stratosphere during days -7 to -2. In contrast, during the same period in PULSE_lag events (Figs. 9b, d), although wave activity fluxes strengthen in the troposphere, they propagate mainly toward the low-pressure center, the East Asian trough within the troposphere, failing to reach the stratosphere above 100 hPa. Accompanying these wave activities, positive and negative anomalies in the troposphere amplify the climatological trough and ridge at days -4 to -2 for PULSE_lag events (Fig. 9d). Then, during days -1 to +1, upward wave activity fluxes intensify in the stratosphere within the East Asian sector, coinciding with a further intensification and upward extension of negative height anomaly into the stratosphere. This anomaly maintains a westward-tilted vertical structure over the following week, superimposing onto the climatological trough, consistent with the strengthening of upward-propagating wave activity fluxes from the troposphere. Therefore, a bottom-up coupling process mediated by upward wave propagation is

dominant in both types of CAO events. Combining the results from Figs. 5c–f and 6c–f, the key distinction lies in the timing, efficiency, and dominant scale of this propagation: wavenumber-2 wave energy enters the stratosphere readily and early in PULSE_lead events, whereas in PULSE_lag events, the combined activity of wavenumber-1 (dominant) and wavenumber-2 waves strengthens and requires a longer period to propagate into the stratosphere.

Interestingly, during 1 week before PULSE_lead events, the main feature in geopotential height anomalies is a nearly vertical, equivalent barotropic structure in the low anomalies (~80−120°E), with the negative maximum located in the stratosphere, above 50 hPa (Figs. 9a, c, e). This seems to suggest a top-down, equivalent barotropic response, which is quite different with those westward-tilted baroclinically amplifying wave structure found in the week after PULSE_lag events. This barotropic structure found before PULSE_lead CAO events raises a question of interest: do precursory stratospheric warm air mass transports exert a downward influence on Asian CAO events, and if so, through what primary pathways might this occur?

4.2 Downward Pathway from PULSE to CAOs of PULSE_lead Type

From the latitude-isentropic distribution of integrated isentropic mass anomalies averaged over three periods (days -7 to -5, -4 to -2, and -1 to +1) in the primary longitudinal range (70–150°E) of the East Asian trough intensification, it can be observed that prior to the occurrence of both PULSE_lead and PULSE_lag type of CAO event, the equatorward transport of cold air in the troposphere is anomalously strong (Figs. 5a, 5b). This results in a significant quadrupole pattern in the daily tropospheric mass anomalies in extratropics, which becomes increasingly pronounced by days -1 to +1 (Figs. 10a–f). Specifically, for cold air below 280 K, positive anomalies dominate at mid-latitudes south of 60°N, while negative anomalies prevail at high latitudes. Opposite can be said for warm tropospheric air above 280 K, indicating that the exchange of cold and warm air triggered by stronger cold branch is the primary mechanism behind the “warm Arctic–cold Eurasian mid-latitudes” pattern

characteristic of Asian CAO events as shown in Fig. 4.

In the stratosphere, for PULSE_lead-type CAO events, anomalously strong poleward warm air transport (reflected by an enhanced ST60N index) is observed about one week before the peak event (Fig. 5a). This corresponds to a distinct pattern in daily stratospheric mass daily tendency anomalies, characterized by an increase at high latitudes and a decrease at mid-latitudes. As a result, negative stratospheric mass anomalies gradually shift southward, reaching their maximum amplitude around days -1 to +1 within the 45–65°N region. These anomalies lie directly above the negative warm air mass anomalies in the mid-latitude troposphere, collectively contributing to the deepening of the East Asian trough. This is consistent with the secondary intensification of East Asian trough around days -1 to +1, observed from Fig. 7e. In contrast, during the early stages of PULSE_lag-type CAO events, which correspond to a weaker ST60N signal, positive mass anomalies prevail in the mid-latitude stratosphere. The accumulated negative mass anomalies above the 280 K isentropic level in the mid-troposphere are less pronounced than in PULSE_lead events. This suggests that, despite the lower air density in the stratosphere, stratospheric mass anomalies still play an important role in the deepening and maintenance of the East Asian trough.

We further quantify the contribution from stratospheric PULSE by examining the joint probability density function (PDF) between two variables: (i) the total air mass anomalies in the stratosphere (above 350K) over the region (45–65°N, 70–150°E), averaged over days -4 to +1, and (ii) ST60N averaged over days -7 to -2 (Fig. 11a). It is seen that for PULSE_lead events (red contours), the joint PDF is confined to the first and fourth quadrants, where ST60N is positive, indicating that the PULSE occurs prior to the CAO event. Large values of joint PDF predominantly concentrate in the fourth quadrant, characterized by the combination of precursory positive ST60N and subsequent negative stratospheric air mass anomalies over the East Asian mid-latitudes, with a total probability of 70%. This suggests that intensified warm air transport into the polar stratosphere results in anomalous stratospheric air mass deficit over the East Asian mid-latitudes. We further examine the joint PDF between the total air mass

anomalies above 350K and those above 290K (i.e., extending down into the md-troposphere) over the same region averaging period (Figure 11b). We found that joint PDF is largely concentrated in the third quadrant, where both stratospheric and tropospheric air mass anomalies are negative. Notably, larger negative anomalies above 350 K correspond to larger negative anomalies above 290 K, indicating a coherent vertical structure. To quantify the stratospheric contribution, we define a contribution ratio as the total air mass anomaly above 350 K divided by that above 290 K. As shown by the right y-axis in Fig. 11b, this contribution ratio reaches up to 0.36, which is read from the shading, suggesting that despite the relative thinness of the stratospheric air, its mass variability makes a non-negligible contribution to the full column above the mid-troposphere, and thereby to the evolution of mid-tropospheric trough–ridge systems. Examining the joint distribution between mass anomalies above 350 K and their contribution ratio (shadings in Fig.11b), we find that the second quadrant, characterized by negative mass anomalies above 350K and a positive contribution ratio to those above 290K, shows a high probability of 62.3%. This indicates that, in PULSE_lead events, the stratospheric mass deficit is not merely a passive response but actively contributes to the total column mass reduction. In contrast, for PULSE_lag events, the absence of a clear shift of PDF toward positive ST60N (Fig. 11a, blue contours) results in stratospheric mass anomalies above 350K are nearly equally split between positive and negative values. Consequently, no clear preference is found for any mass-ratio quadrant (Figure 11c). These results demonstrate that, unlike PULSE_lag events, in the early stage of PULSE_lead events, the PULSE signal is not merely a stratospheric imprint of rapidly propagating tropospheric wavenumber-2 waves. Instead, it acts to enhance poleward warm air transport over East Asia, leading to a reduction in mid-latitude air mass and lowered pressure, which in turn plays an important role in deepening and maintaining the East Asian trough, while the intensification of this trough is one of the key large-scale tropospheric circulation systems responsible for the formation of Asian CAO events.

5 Conclusion and Discussion

5.1 Conclusions

This study presents an objective classification of wintertime CAO events in midlatitude Asia based on their temporal phasing with pulse-like intensification of stratospheric poleward warm air transport (PULSE). By applying lagged EOF analysis to the ST60N index in the two weeks centered at the peak dates of 173 CAO events from 1979 to 2024, we identified two distinct types: PULSE_lead events (18.0%), where the stratospheric PULSE precedes the CAO peak, and PULSE_lag events (21.4%), where the PULSE follows it. While both types exhibit similar peak intensity in terms of cold area coverage and no significant difference in the magnitude of low-temperature anomalies, PULSE_lead events are characterized by averagely longer persistence and a more widespread spatial extent of cold anomalies across Eurasia, thus posing a greater potential socioeconomic threat.

Our findings reveal the dynamical origins of these distinct temporal phasing relationships. From an isentropic meridional mass circulation perspective, the temporal phasing is fundamentally governed by the coupling between the stratospheric warm branch and tropospheric cold branch of the isentropic meridional mass circulation at 60°N. The enhanced poleward warm air transport over the Northwestern Pacific dominates the intensification of stratospheric warm branch while the intensified equatorward cold air transport in the lower troposphere across Asia dominates the intensification of cold branch. When these two branches are simultaneously intensified, PULSE_lead events occur, whereas when stratospheric warm air transport lags tropospheric cold air transport by more than one week, PULSE_lag events develop. Wave decomposition and stratospheric-tropospheric circulation analysis demonstrate that during PULSE_lead events, accompanied with the intensification of Ural ridge, increased wave energy (predominantly wavenumber-2) rapidly propagates upward into the stratosphere ahead of the CAO peak, driving the precursory PULSE. Conversely, in PULSE_lag events, wave energy associated with a more remarkbly intensified Ural

ridge propagates mainly eastward within the troposphere, amplifying the East Asian trough downstream and triggering the CAO first, followed by delayed upward propagation of combined wavenumber-1 (dominant) and wavenumber-2 energy that induces the stratospheric response. The more efficient wave propagation in PULSE_lead events appears to be related to pre-existing polar vortex that shifts toward the Asian sector.

Results further demonstrate that for PULSE_lead events, the precursory stratospheric PULSE signal is not merely a passive imprint. The early, wavenumber-2-driven PULSE leads to a significant reduction of air mass in the midlatitude stratosphere over East Asia, approximately the East Asian trough region. This stratospheric mass deficit contributes up to 0.36 of the total mass changes above the mid-troposphere, deepening and maintaining the East Asian trough. Such a stratospheric downward influence through stratospheric mass deficit mechanism occurs in 62.3% of the PULSE_lead CAOs. This explains why with a comparatively weaker Ural Ridge compared to PULSE_lag type, we can observe a more persistent and vertically barotropic East Asian trough anomaly, which creates a favorable large-scale circulation pattern that amplifies and sustains the subsequent CAO. This represents a downward influence pathway from the stratospheric PULSE to the tropospheric CAO over Asia.

In conclusion, by distinguishing between CAOs with and without precursory stratospheric PULSEs, our results help reconcile seemingly contradictory findings in the literature. The common observation that Asian CAO often precedes weak SPV or PULSE events, as recorded in Kolstad et al. (2010), Woo et al. (2015) and Choi et al. (2021), is consistent with our PULSE_lag type, which is often associated with wavenumber-1 dynamics. On the other hand, the notable counterexamples of severe CAOs following stratospheric disturbances, such as those in the 2020/21 winter accompanied with a split-type SSW (Yu et al. 2021; Zhang et al. 2022; Davis et al. 2022), align with the PULSE_lead type driven by wavenumber-2. By demonstrating that only a subset of CAOs (18%) involves active stratospheric pulse-like precursors, our findings clarify that these two perspectives are not mutually exclusive. In fact, they reflect different subsets of events with distinct formation mechanisms.

Rather than overgeneralizing the role of stratospheric downward influence in Asian CAOs, we highlight that a precursory, wavenumber-2-driven intensification of the stratospheric warm air mass transport into the polar stratosphere (ST60N_W2) can contribute to a subset of Asian CAOs through a downward-influencing mass deficit mechanism. Then one may ask whether this signal offers a promising source of predictability at extended ranges. According to Yu et al. (2019), operational forecast models such as CFSv2 can provide up to 17 and 11 days of lead prediction for positive ST60N_W2 events when a 2-day and 1-day time shift is allowed, respectively. This suggests that, for Asia, the use of precursory PULSE signals in stratospheric poleward warm air transport in sub-seasonal CAO forecasts may be feasible. However, it must be acknowledged that the applicability of this forecast pathway is inherently limited, as only a moderate fraction of CAO events exhibit precursory PULSE signals.

5.2 Discussions

Although the 78 identified PULSE-related CAO events account for approximately 40% of all Asian CAOs, the remaining majority are associated with the negative phases of the leading EOF modes, corresponding to a less disturbed stratosphere and a stronger polar vortex. A next step would be to evaluate the practical forecast skill for these two distinct CAO types, in comparison to troposphere-only events, using state-of-the-art sub-seasonal prediction models. Such an assessment is crucial for translating the present dynamical understanding into improved operational forecasting capabilities.

Moreover, given that our analysis suggests a pre-existing Asian-shifted polar vortex is critical for establishing a stratospheric pathway and forming a precursory PULSE signal before CAOs, we further trace the earlier evolution of the stratospheric polar vortex. As shown in Figs. 12a–b, significant geopotential height anomalies at 50 hPa are evident as early as two weeks prior to both event types. For PULSE_lead events, a significant negative anomaly in high latitudes (50–80°N) accompanied by stronger westerlies at 50°N is observed near North America beginning 15 days before the event. A negative anomaly also emerges over Asia around day –11. Combined with the spatial

pattern in Fig. 12c, this indicates an elongation and stretching of the polar vortex, a pattern consistent with existing literature (Park et al. 2014; Garfinkel et al. 2017; Zhang et al. 2022; Huang et al. 2025). Distinctively, the two weeks preceding PULSE_lag events are characterized by negative anomalies over high-latitude North America and positive anomalies over high-latitude Europe and Central Asia. This pattern indicates a shift of the polar vortex toward North America preceding PULSE_lag CAOs. Subsequently, from the CAO peak to two weeks after, the anomaly pattern reverses completely. This evolution implies the presence of a quasi-periodic oscillation in the stratospheric circulation, aligning with the earlier work of Shen et al. (2023). It is also similar to the stratospheric signals associated with North American reflective events (Kolstad et al. 2010; Woo et al. 2015; Yu et al. 2024). It is noteworthy to point out that previous studies have linked wave-train–type CAOs to the formation of a negative upper-tropospheric height anomaly southeast of Greenland approximately 12 days in advance, a signal potentially originating from the lower stratosphere over the North Atlantic (Cohen et al. 2010; Orsolini et al. 2016). This anomaly is observed in both types of PULSE-related CAOs in present study, suggesting that such a precursor, by itself, is insufficient to determine whether a subsequent CAO will be dynamically influenced by stratospheric downward propagation. This insight is corroborated by Shen et al. (2025), who reported that Eurasian cold events with similar local tropospheric circulations can exhibit divergent large-scale evolution, with only a subset being linked to the stratosphere.

Our primary investigation also yields that the annual occurrence of PULSE_lead CAO events exhibits no significant long-term trend, suggesting weak influence from AA-related changes; instead, it is dominated by interannual variability, with a period of approximately 3 years accounting for 65.2% of the total variance, as identified by ensemble empirical mode decomposition (EEMD, Feng et al., 2014). Correlation analysis with external forcings indicates that these events are significantly correlated with linearly detrended Autumn sea ice concentration anomalies in Barents sea ($r=-0.302$) and La Niña like sea surface temperature anomaly pattern ($r=-0.325$). This is consistent with existing findings; for instance, Arctic sea ice loss in the Barents-Kara

Seas prolongs CAO duration through stratosphere-troposphere wave feedbacks (Deser et al. 2016; Zhang et al. 2022; Davis et al. 2022), while La Niña conditions can favor certain planetary wave configurations that modulate stratospheric pathways (Hu et al. 2017; Zhang et al. 2022). Such pre-conditioning of the stratospheric polar vortex and its drivers need further investigation. This is important because identifying the large-scale conditions favoring PULSE_lead-type CAOs at a longer lead time would enable early indication of whether an impending CAO is likely to follow the PULSE_lead evolution pathway. In turn, this would allow for more informed utilization of ST60N_W2-based forecasts to anticipate subsequent occurrence of CAOs in midlatitude Asia.

References

Baldwin, M. P., and T. J. Dunkerton (1999) Propagation of the arctic oscillation from the stratosphere to the troposphere. *J. Geophys. Res*., 104(D24), 30937-30946, https://doi.org/10.1029/1999JD900445.

Cai, M. (2003) Potential vorticity intrusion index and climate variability of surface temperature. *Geophys. Res. Lett*., 30, 1119, https://doi.org/10.1029/2002GL015926.

Cai, M., and R. Ren (2007) Meridional and Downward Propagation of Atmospheric Circulation Anomalies. Part I: Northern Hemisphere Cold Season Variability. *J. Atmos. Sci*., 64, 1880–1901, https://doi.org/10.1175/JAS3922.1.

Cai, M., and C. S. Shin (2014) A Total Flow Perspective of Atmospheric Mass and Angular Momentum Circulations: Boreal Winter Mean State. *J. Atmos. Sci*., 71, 2244–2263, https://doi.org/10.1175/JAS-D-13-0175.1.

Cai, M., Y. Yu, Y. Deng, H. M. van den Dool, R. Ren, S. Saha, X. Wu, and J. Huang (2016) Feeling the Pulse of the Stratosphere: An Emerging Opportunity for Predicting Continental-Scale Cold-Air Outbreaks 1 Month in Advance. *Bull. Amer. Meteorol. Soc.*, 97, 1475–1489, https://doi.org/10.1175/BAMS-D-14-00287.1.

Cheung, H. N., W. Zhou, H. Y. Mok, and M. C. Wu (2012) Relationship between Ural–Siberian Blocking and the East Asian Winter Monsoon in Relation to the Arctic Oscillation and the El Niño–Southern Oscillation. *J. Clim*., 25, 4242–4257, https://doi.org/10.1175/JCLI-D-11-00225.1.

Chen, T., W. Huang, and J. Yoon (2004) Interannual variation of the East Asian cold surge activity. J. Clim., 17, 401–413, https://doi.org/10.1175/1520-0442(2004)017,0401:IVOTEA.2.0.CO;2.

Choi H., J. H. Kim, B. M. Kim, and S. J. Kim (2021) Observational evidence of distinguishable weather patterns for three types of sudden stratospheric warming during northern winter. *Front. Earth Sci.*, 9, 625868, https://doi.org/10.3389/feart.2021.625868.

Cholaw, B., Z. Anran, Z. Xie, M. Yong, and P. Gomboluudev (2022) The development of a powerful Mongolian cyclone on 14–15 March 2021: Eddy energy analysis. *Atmos. Oceanic Sci. Lett*., 15(6), 1674-2834, https://doi.org/10.1016/j.aosl.2022.100259.

Cohen, J., K. Saito, and D. Entekhabi (2001) The role of the Siberian high in Northern Hemisphere climate variability. *Geophys. Res. Lett*., 28, 299-302, https://doi.org/10.1029/2000GL011927.

Cohen, J., J. Foster, M. Barlow, K. Saito, and J. Jones (2010) Winter 2009–2010: A case study of an extreme Arctic Oscillation event. *Geophys. Res. Lett.*, 37, L17707, https://doi.org/10.1029/2010GL044256.

Cohen, J., Screen, J., Furtado, J. et al. (2014) Recent Arctic amplification and extreme mid-latitude weather. *Nature Geosci*., 7. 627–637, https://doi.org/10.1038/ngeo2234.

Davis, N. A., J. H. Richter, A. A. Glanville, J. Edwards, and E. LaJoie (2022) Limited surface impacts of

694 the January 2021 sudden stratospheric warming. *Nat. Commun*., 13, 1136,
695 https://doi.org/10.1038/s41467-022-28836-1.
696 Dasgupta, P. and M. K. Roxy, R. Chattopadhyay, et al. (2021) Interannual variability of the frequency of
697 MJO phases and its association with two types of ENSO. *Sci. Rep.*, 11, 11541,
698 https://doi.org/10.1038/s41598-021-91060-2.
699 Deng, J., and H. Xu (2024) Modulation effects of the Tibetan-Mongolian Plateaus on East Asian winter
700 air temperature associated with synoptic evolution of Siberian high. *Clim. Dyn*., 62, 9469-9488,
701 https://doi.org/10.1007/s00382-024-07404-x.
702 Deser, C., L. Sun, R. A. Tomas, and J. A. Screen (2016) Does ocean coupling matter for the northern
703 extratropical response to projected Arctic sea ice loss? *Geophys. Res. Lett.*, 43, 2149–2157,
704 https://doi.org/10.1002/2016GL067792.
705 Domeisen, D. I. V., A. H. Butler, A. J. Charlton-Perez, B. Ayarzagüena, M. P. Baldwin, E. Dunn-Sigouin,
706 et al. (2020) The role of the stratosphere in subseasonal to seasonal prediction: 1. Predictability of
707 the stratosphere. *J. Geophys. Res-Atmos*., 125, e2019JD030920,
708 https://doi.org/10.1029/2019JD030920.
709 Dong, Z., L. Wang, S. Gui, H. Gong, and K. Hu (2023) Diminished impact of the East Asian winter
710 monsoon on the maritime continent rainfall after the late-1990s tied to weakened Siberian high–
711 Aleutian low Covariation. *J. Geophys. Res-Atmos*., 128, e2022JD037336,
712 https://doi.org/10.1029/2022JD037336.
713 Dunn-Sigouin, E., and T. Shaw (2020) Dynamics of Anomalous Stratospheric Eddy Heat Flux Events in
714 an Idealized Model. *J. Atmos. Sci*., 77, 2187–2202, https://doi.org/10.1175/JAS-D-19-0231.1.
715 Feng, J., Z. Wu, and G. Liu (2014) Fast Multidimensional Ensemble Empirical Mode Decomposition
716 Using a Data Compression Technique. *J. Climate*, 27, 3492–3504, https://doi.org/10.1175/JCLI-
717 D-13-00746.1.
718 Francis, A., and J. Vavrus (2012) Evidence linking Arctic amplification to extreme weather in mid-
719 latitudes. *Geophys. Res. Lett.*, 39, L06801, https://doi.org/10.1029/2012GL051000.
720 Francis, A., J. Vavrus, and J. Cohen (2017) Amplified Arctic warming and mid-latitude weather: new
721 perspectives on emerging connections. WIREs. *Clim. Change*, 8, e474,
722 https://doi.org/10.1002/wcc.474.
723 Garfinkel, C. I., S. W. Son,, K. Song, et al. (2017) Stratospheric variability contributed to and sustained
724 the recent hiatus in Eurasian winter warming. *Geophys. Res. Lett.*, 44, 374–382,
725 https://doi.org/10.1002/2016GL072035.
726 Gong, H., L. Wang, W. Chen, and R. Wu (2019) Attribution of the East Asian winter temperature trends
727 during 1979–2018: Role of external forcing and internal variability. *Geophys. Res. Lett.*, 46,
728 10875–10882, https://doi.org/10.1029/2019GL084154.

729 Gong, H., L. Wang, W. Chen, and R. Wu (2019) Time‐varying contribution of internal dynamics to
730 wintertime land temperature trends over the Northern Hemisphere. *Geophys. Res. Lett.*, 46,
731 https://doi.org/10.1029/2019GL086220.
732 Gong, H., H. Xiao, Q. Chen, and L. Wang (2022) Impact of internal climate variability on wintertime
733 surface air temperature trends over Eurasia in the CESM1 large ensemble. *J. Geophys. Res-Atmos.*,
734 127, e2021JD035340. https://doi.org/10.1029/2021JD035340.
735 Gong, H., K. Ma, L. Wang, and W. Chen (2024) Attribution of the record-breakingextreme cold event
736 over Northern East Asia in December 2023. *Geophys. Res. Lett.*, 51, e2024GL112568,
737 https://doi.org/10.1029/2024GL112568.
738 Gong, H., Wang, L., James A. Screen, Chen, W., Judah Cohen, and Wu, R. (2025) Teleconnection from
739 Arctic warming suppresses long-term warming in centralEurasia. *Sci. Adv.*, 11, (12),
740 https://www.science.org/doi/10.1126/sciadv.adq9461.
741 Hersbach, H., Bell, B., Berrisford, P., Hirahara, S., Horanyi, A., Munoz-Sabater, J., et al. (2020) The
742 ERA5 global reanalysis. *Quarterly Journal of the Royal Meteorological Society*, 146, 1999–2049.
743 https://doi.org/10.1002/qj.3803.
744 Hu, J., T. Li, H. Xu, et al. (2017) Lessened response of boreal winter stratospheric polar vortex to El Niño
745 in recent decades. *Clim. Dyn*., 49, 263–278, https://doi.org/10.1007/s00382-016-3340-z.
746 Huang, Z., Y. Huang, Z. Yin, and H. Wang (2025) Subseasonal reversal of extreme cold temperature
747 frequencies in Northeast China: Possible mechanism and prediction. *J. Geophys. Res-Atmos.*, 130,
748 e2024JD042556, https://doi.org/10.1029/2024JD042556.
749 Hwang, J., S. W. Son, P. Martineau, et al. (2022) Impact of winter blocking on surface air temperature in
750 East Asia: Ural versus Okhotsk blocking. *Clim. Dyn.*, 59, 2197–2212,
751 https://doi.org/10.1007/s00382-022-06204-5.
752 Iwasaki, T. and Y. Mochizuki (2012) Mass-weighted isentropic zonal mean equatorward flow in the
753 Northern Hemispheric winter. *SOLA*., 8, 115–118, https://doi.org/10.2151/sola.2012-029.
754 Johnson, D. R. (1989) The forcing and maintenance of global monsoonal circulations: An isentropic
755 analysis. *Adv. Geophys*., 31, 43–316, https://doi.org/10.1016/S0065-2687(08)60053-9.
756 Kidston, J., A. A. Scaife, S. C. Hardiman, et al. (2015) Stratospheric influence on tropospheric jet streams,
757 storm tracks and surface weather. *Nature Geosci*., 8, 433–440, https://doi.org/10.1038/ngeo2424.
758 Kolstad, E. W., T. Breiteig, and A. A. Scaife (2010) The association between stratospheric weak polar
759 vortex events and cold air outbreaks in the Northern Hemisphere. *Q. J. R. Meteorol. Soc*., 136, 886–
760 893, https://doi.org/10.1002/qj.620.
761 Kuttippurath, J., and G. Nikulin (2012) A comparative study of the major sudden stratospheric warmings
762 in the Arctic winters 2003/2004–2009/2010. *A.C.P.*, 12, 8115–8129, https://doi.org/10.5194/acp-12-
763 8115-2012.

764 Lehtonen, I. and A. Y. Karpechko (2016) Observed and modeled tropospheric cold anomalies associated
765 with sudden stratospheric warmings. *J. Geophys. Res-Atmos*., 121, 1591–1610,
766 https://doi.org/10.1002/2015JD023860.
767 Li, D., T. Zhou, Y. Qi, L. Zou, et al. (2024) Future reduction of cold extremes over East Asia due to
768 thermodynamic and dynamic warming. *A.C.P.*, 24, 7347–7358, https://doi.org/10.5194/acp-24-
769 7347-2024.
770 Lim, Y. K. and H. D. Kim (2013) Impact of the dominant large-scale teleconnections on winter
771 temperature variability over East Asia. *J. Geophys. Res-Atmos*., 118, 7835-7848,
772 https://doi.org/10.1002/jgrd.50462.
773 Lin, H., B. Yu, and N. M. J. Hall (2025) Link of the Warm Arctic Cold Eurasian pattern to the Southern
774 Annular Mode variability. *npj Clim. Atmos. Sci.*, 8, 225, https://doi.org/10.1038/s41612-025-01102-
775 z.
776 Liu, Y., L. Wang, W. Zhou, et al. (2014) Three Eurasian teleconnection patterns: spatial structures,
777 temporal variability, and associated winter climate anomalies. *Clim. Dyn*., 42, 2817–2839,
778 https://doi.org/10.1007/s00382-014-2163-z.
779 Maeda, S., K. Takemura, and C. Kobayashi (2021) Planetary Wave Modulations Associated with the
780 Eurasian Teleconnection Pattern. *J. Meteorol. Soc. Jpn*., 99(2), 449-458,
781 https://doi.org/10.2151/jmsj.2021-022.
782 Mayer, K. J., W. E. Chapman, and W. A. Manriquez (2024) Exploring the relative importance of the MJO
783 and ENSO to North Pacific subseasonal predictability. *Geophys. Res. Lett.*, 51, e2024GL108479,
784 https://doi.org/10.1029/2024GL108479.
785 Miao, J. and T. Wang (2020) Decadal variations of the East Asian winter monsoon in recent decades.
786 *Atmos. Sci. Lett.*, 21, e960, https://doi.org/10.1002/asl.960.
787 Orsolini, Y. J., R. Senan, F. Vitart, et al. (2016) Influence of the Eurasian snow on the negative North
788 Atlantic Oscillation in subseasonal forecasts of the cold winter 2009/2010. *Clim. Dyn*., 47, 1325–
789 1334, https://doi.org/10.1007/s00382-015-2903-8.
790 Park, T. W., C. H. Ho, J. H. Jeong, et al. (2015) A new dynamical index for classification of cold surge
791 types over East Asia. *Clim. Dyn.*, 45, 2469–2484, https://doi.org/10.1007/s00382-015-2483-7.
792 Park, T. W., C. H. Ho, and Y. Deng (2014) A synoptic and dynamical characterization of wave-train and
793 blocking cold surge over East Asia. *Clim. Dyn*., 43, 753–770, https://doi.org/10.1007/s00382-013-
794 1817-6.
795 Park, H. J., J. B. Ahn (2016) Combined effect of the Arctic Oscillation and the Western Pacific pattern
796 on East Asia winter temperature. *Clim. Dyn.,* 46, 3205–3221, https://doi.org/10.1007/s00382-015-
797 2763-2.
798 Polvani, M., and W. Waugh (2004) Upward Wave Activity Flux as a Precursor to Extreme Stratospheric

Events and Subsequent Anomalous Surface Weather Regimes. *J. Clim.*, 17. 3548-3554, https://doi.org/10.1175/1520-0442(2004)017<3548:UWAFAA>2.0.CO;2.

Shen, X., Wang, L., Scaife, A. A., Hardiman, S. C., and Xu, P. (2023) The Stratosphere-Troposphere Oscillation as the dominant intraseasonal coupling mode between the stratosphere and troposphere. *J. Clim.*, 36, 2259–2276, https://doi.org/10.1175/jcli-d-22-0238.

Shen, X., Wang, L., Scaife, A. A., & Hardiman, S. C. (2025) Intraseasonal linkages of winter surface air temperature between Eurasia and North America. *Geophysical Research Letters*, 52, e2024GL113301, https://doi.org/10.1029/2024GL113301.

Shi, S., T. Zhang, Z. Ma, W. Li, Y. Yang, and S. Yang (2020) Study on variation characteristics of frequency of cold wave processes in the northeastern Qinghai-Tibet Plateau. *J. Glaciol*., 42(4), 1169-1178, https://doi.org/10.7522/j.issn.1000-0240.2020.0099.

Simmons, A. J., and A. Hollingsworth (2002) Some aspects of the improvement in skill of numerical weather prediction. *Q. J. R. Meteorol. Soc.*, 128, 647–677, https://doi.org/10.1256/003590002321042135.

Sorokina, S. A., C. Li, J. J. Wettstein, and N. G. Kvamstø (2016) Observed Atmospheric Coupling between Barents Sea Ice and the Warm-Arctic Cold-Siberian Anomaly Pattern. *J. Clim*., 29, 495–511, https://doi.org/10.1175/JCLI-D-15-0046.1.

Takaya, K., and H. Nakamura (2001) A Formulation of a Phase-Independent Wave-Activity Flux for Stationary and Migratory Quasigeostrophic Eddies on a Zonally Varying Basic Flow. *J. Atmos. Sci*., 58, 608–627, https://doi.org/10.1175/1520-0469(2001)058<0608:AFOAPI>2.0.CO;2.

Thompson, D. W., M. P. Baldwin, and J. M. Wallace (2002) Stratospheric connection to Northern Hemisphere wintertime weather: Implications for prediction. *J. Clim.*, 15, 1421–1428, https://doi.org/10.1175/1520-0442(2002)015<1421:SCTNHW>2.0.CO;2.

Tripathi, O. P., M. Baldwin, A. Charlton-Perez, et al. (2015) The predictability of the extratropical stratosphere on monthly time-scales and its impact on the skill of tropospheric forecasts. *Q. J. R. Meteorol. Soc*., 141, 987-1003, https://doi.org/10.1002/qj.2432.

Wu, B., and J. Wang (2002) Winter Arctic Oscillation, Siberian high and East Asian winter monsoon. *Geophys. Res. Lett.*, 29(19), 31-34, https://doi.org/10.1029/2002GL015373.

Woo, S., B. Kim, and J. Kug (2015) Temperature Variation over East Asia during the Lifecycle of Weak Stratospheric Polar Vortex. *J. Clim*., 28, 5857–5872, https://doi.org/10.1175/JCLI-D-14-00790.1.

Yang, Y. F., Y. Y. Yu, C. H. Shi, et al (2025) Temporal phasing of stronger warm air mass transport into the polar stratosphere and cold air outbreaks in North America. *J. Meteorol. Res.*, 39(5), 1-18, https://doi.org/10.1007/s13351-025-5037-x.

Yu, Y., R. Ren, J. Hu, and G. Wu (2014) A mass budget analysis on the interannual variability of the polar surface pressure in the winter season. *J. Atmos. Sci.*, 71(9), 3539–3553, https://doi.org/10.1175/JAS-

D-13-0365.1.

Yu, Y., M. Cai, R. Ren, and H. M. Van Den Dool (2015a) Relationship between warm airmass transport into the upper polar atmosphere and cold air outbreaks in winter. *J. Atmos. Sci.*, 72(1), 349–368, https://doi.org/10.1175/JAS-D-14-0111.1.

Yu, Y., R. Ren, and M. Cai (2015b) Dynamic linkage between cold air outbreaks and intensity variations of the meridional mass circulation. *J. Atmos. Sci.*, 72 (8), 3214–3232, https://doi.org/10.1175/JAS-D-14-0390.1.

Yu, Y., M. Cai, C. Shi, and R. Ren (2018a) On the linkage among strong stratospheric mass circulation, stratospheric sudden warming, and cold weather events. *Mon. Weather Rev.*, 146(9), 2717–2739, https://doi.org/10.1175/MWR-D-18-0110.1.

Yu, Y., M. Cai, and R. Ren (2018b) A stochastic model with a low-frequency amplification feedback for the stratospheric northern annular mode. *Clim. Dyn.*, 50(9), 3757–3773, https://doi.org/10.1007/s00382-017-3843-2.

Yu, Y., M. Cai, R. Ren, and J. Rao (2018c) A closer look at the relationships between meridional mass circulation pulses in the stratosphere and cold air outbreak patterns in northern hemispheric winter. *Clim. Dyn.*, 51(7), 3125–3143, https://doi.org/10.1007/s00382-018-4069-7.

Yu, Y. and Ren, R. (2019) Understanding the variation of stratosphere–troposphere coupling during stratospheric northern annular mode events from a mass circulation perspective. *Clim. Dyn.*, 53, 5141–5164, https://doi.org/10.1007/s00382-019-04675-7.

Yu, Y., M. Cai,, C. Shi, et al. (2019) Sub-seasonal prediction skill for the stratospheric meridional mass circulation variability in CFSv2. *Clim. Dyn*., 53, 631–650, https://doi.org/10.1007/s00382-018-04609-9.

Yu, Y. Y., Y. F. Li, R. C. Ren, M. Cai, et al. (2021) An Isentropic Mass Circulation View on the Extreme Cold Events in 2020/2021 Winter. *Adv. Atmos. Sci*, 39, 643–657, https://doi.org/10.1007/s00376-021-1289-2.

Yu, Y., L. Bowen, R. Rongcai, G. Zhaoyong, Y. Qinlan, and H. Muxin (2022) Precursory Signals in the Stratospheric Meridional Mass Circulation for Mid-Latitude Cold Air Outbreak Events of High and Low Sub-Seasonal Predictability. *J. Geophys. Res-Atmos*., 127, 16, https://doi.org/10.1029/2022JD036814.

Yu, Y., X. Yu, Z. Guan, D. Hu, C. Shi, D. Guo, and J. Rao (2023) Stratospheric PULSE–continental cold air outbreak coupling relationships: Interannual and interdecadal changes. *Front. Earth Sci.*, 10, 1093189, https://doi.org/10.3389/feart.2022.1093189.

Yu, Y., R. Ren, Y. Li, et al. (2024) Continental cold-air-outbreaks under the varying stratosphere-troposphere coupling regimes during stratospheric Northern Annular Mode events. *Clim. Dyn*., 62, 7207–7231, https://doi.org/10.1007/s00382-024-07275-2.

Zhang, L. and C. Lu (2022) Detection of the synoptic southeastward-extending Siberian cold high during 1978–2017. Atmos. Oceanic *Sci. Lett*., 15(3), 1674-2834, https://doi.org/10.1016/j.aosl.2021.100140.

Zhang, F., Y. Q. Sun, L. Magnusson, R. Buizza, S. Lin, J. Chen, and K. Emanuel (2019) What Is the Predictability Limit of Midlatitude Weather?. *J. Atmos. Sci*., 76, 1077–1091, https://doi.org/10.1175/JAS-D-18-0269.1.

Zhang, X., Rao, J., Garfinkel, C. I., Son, S.-W., He, B., and Liu, Y. (2025). Classification of cold air outbreaks in East Asia and potential stratospheric harbingers. *J. Geophys. Res-Atmos*., 130, e2024JD043199.

Zhang, R. N., R. H. Zhang, and C. Sun (2022) Modulation of the interdecadal variation of atmospheric background flow on the recent recovery of the EAWM during the 2000s and its link with North Atlantic–Arctic warming. *Clim. Dyn*.. 59, 561–578, https://doi.org/10.1007/s00382-022-06152-0.

Zhang, R., W. Zhou, W. Tian, Y. Zhang, Z. Liu, and P. K. Y. Cheung (2022) Changes in the Relationship between ENSO and the Winter Arctic Stratospheric Polar Vortex in Recent Decades. *J. Clim.*, 35, 5399–5414, https://doi.org/10.1175/JCLI-D-21-0924.1.

Zou, C., R. Zhang, P. Zhang, L. Wang, and R. Zhang (2024) Contrasting physical mechanisms linking stratospheric polar vortex stretching events to cold Eurasia between autumn and late winter. *Clim. Dyn*., 62, 2399-2417, https://doi.org/10.1007/s00382-023-07030-z.

Zou, C. and R. Zhang (2024) Arctic sea ice loss modulates the surface impact of autumn stratospheric polar vortex stretching events. *Geophys. Res. Lett*., 51, e2023GL107221, https://doi.org/10.1029/2023GL107221.

Acknowledgments

This research was jointly supported by National Natural Science Foundation of China, Grant/Award Numbers: 42375060.

Statements and Declarations

Funding

This work is supported by the National Natural Science Foundation of China (grant 42375060)

Competing interests

The authors have no relevant financial or non-financial interests to disclose.

Author Contributions

Zhiqiang Ding contributed to do the analyses, made the figures and wrote the first draft of the paper. Yueyue Yu formulated the main ideas, contributed to the design of the analyses, and helped review and editing the manuscript. Haishan Chen, Xiaocen Shen, Ming Cai, Yang Liu helped review and editing the manuscript.

Data availability

The ERA5 datasets used in this study are obtained from the official websites (https://cds.climate.copernicus.eu/datasets/derived-era5-single-levels-daily-statistics; https://cds.climate.copernicus.eu/datasets/derived-era5-pressure-levels-daily-statistics).

Author information

Authors and Affiliations

State Key Laboratory of Environment Characteristics and Effects for Near-space, Nanjing 210044, China

Zhiqiang Ding, Yueyue Yu & Yang Liu

State Key Laboratory of Climate System Prediction and Risk Management, Nanjing 210044, China

Haishan Chen

Ministry of Education/Collaborative Innovation Center on Forecast and Evaluation of Meteorological Disasters, Nanjing University of Information Science and Technology, Nanjing 210044, China

Zhiqiang Ding, Yueyue Yu, Haishan Chen & Yang Liu

Department of Meteorology, University of Reading, Reading, UK

Xiaocen Shen

Department of Earth, Ocean Atmospheric Sciences, Florida State University, Tallahassee, FL 32304, USA

Ming Cai

Corresponding author

Correspondence to YueyueYu.

Ethics declarations

Conflict of interest

The authors declare no potential conflict of interest.

Consent for publication

All the authors agree the submission and publication of the paper.

Additional information

Publisher's Note

Springer Nature remains neutral with regard to jurisdictional claims in published maps and institutional affiliations.

Captions

Fig. 1 Fourier power spectra of (a) ST60N (units: 1) and (b) ACAP (units: %) index in winters (November–March) from 1979 to 2024.This period serves as the common analysis time frame for all subsequent figures

Fig. 2 Composite of the ACAP index (bars, units: %) and ST60N index and its wavenumber-1 and wavenumber-2 components (lines) during the ±7-day windows centered on peak dates of CAOs: (a) all events, (b) PULSE_lead type events, and (c) PULSE_lag type events. Dots and filled symbols denote statistical significance at the 95% confidence level. The 50^{th} and 70^{th} percentile of ACAP index are highlighted by the horizontal dashed line

Fig. 3 Dominant evolution patterns of ST60N, indicated by the spatial patterns of (a) the first and (b) the second EOF modes for the ST60N index during the ±7-day windows centered on peak dates of 173 Asian CAOs. The percentage of explained variance for each mode is labeled above respective panel

Fig. 4 Spatial distribution of the occurrence probability (shading; units: %) of grid points with 2m temperature anomalies below -0.5 (a – b) and -1.0 (c – d) local standard deviation (LSD) thresholds during all days when the ACAP index exceeds its 50^{th} percentile for CAO events belonging to "PULSE_lead" (a, c), "PULSE_lag" (b, d) types. Probability differences relative to all winter days are overlaid as contours

Fig. 5 Composite isentropic meridional mass flux anomalies at 60°N (shadings, 10^9 kg s^{-1}) averaged over days -6 to 0 (a, c, e) and days +1 to +7 (b, d, f) relative to peak dates of Asian CAO events belonging to PULSE_lead type: total (a – b), wavenumber-1 (c – d) and wavenumber-2 components (e–f). Contours depicts winter climatological mean and right panels display zonal integrated anomalies which above 330K was multiplied by 5 for visualization. Hatched area and colored bars are significant at 95% confidence level

Fig. 6 As in Figure 5, but for PULSE_lag type

Fig. 7 Composite maps of 500 hPa geopotential height anomalies (shading, gpm) and horizontal

wave activity flux (arrows, m^2/s^2) for PULSE-lead and PULSE-lag CAOs relative to their peak dates. Five temporal phases are analyzed: lead times of −7 to −5 days (a–b), −4 to −2 days (c–d), −1 to +1 days (e–f), lag times of +2 to +4 days (g–h), and +5 to +7 days (i–j). All arrows and hatched areas denote statistical significance at the 95% confidence level

Fig. 8 Composite fields of 50 hPa geopotential height anomalies (contours, units: gpm), vertical wave activity flux anomalies at 100 hPa (shading, normalized by time), and horizontal wave activity flux at 100 hPa (arrows, units: m^2/s^2) for PULSE-lead and PULSE-lag CAOs: days −7 to −5 (a–b), days −4 to −2 (c–d), days −1 to +1 (e–f), days +2 to +4 (g–h), and days +5 to +7 (i–j) relative to peak dates. Bold contours indicate statistical significance at the 95% confidence level, and only significant wave fluxes are displayed

Fig. 9 Composite evolution of T-N flux anomaly vectors (zonal and vertical components; units: m^2/s^2) and geopotential height anomaly (shading; units: gpm) averaged over 45–65°N for five periods of (a) PULSE-lead and (b) PULSE-lag CAOs. The climatological winter mean geopotential height (contours; units: gpm) is overlaid. Only anomalies statistically significant at the 95% confidence level are displayed. The levels above 200 hPa is magnified by a factor of three for visualization

Fig. 10 Zonal sum of isentropic mass anomalies (contours, units: 10^{12} kg) over the longitude band 70–150°E and their vertically integral above each isentropic level (shading, units: 10^{12} kg) for PULSE-lead (left column) and PULSE-lag (right column) CAOs during three periods relative to the peak dates: days -7 to -5 (a, b), -4 to -2 (c, d), and -1 to +1 (e, f). The rightmost attached panels display the daily tendency of mass anomalies (units: 10^{12} kg; levels above 350K are amplified by 5), summed over midlatitudes (45–65°N, red curve) and high latitudes (70–90°N, blue curve), respectively. Hatched area, thickened contours and dotted curves denote statistical significance at the 95% confidence level. The solid green line represents the climatological winter mean thermodynamic tropopause potential temperature

Fig. 11 Joint probability distributions (contours, %) of key dynamical and thermodynamical anomalies associated with CAO events. (a) ST60N during days -7 to -2 relative to peak dates versus regionally integrated isentropic mass anomalies above 350K in the low-pressure anomaly key region (45–

65°N, 70–150°E; averaged over days -4 to +1). (b, c) Joint distributions of mass anomalies above 350 K versus (i) those above 290K (contours) and (ii) their ratio (350K/290K; shadings) for the same period (days -4 to +1 relative to peak dates of (b) PULSE_lead and (c) PULSE_lag events). Quadrants labels indicate the probability of samples falling within each bin of the 350 K mass anomaly versus the 350 K/290 K ratio

Fig. 12 Composite of (a, b) 50hPa geopotential height anomalies (shading, units: gpm) averaged over 50°N–80°N and zonal wind anomalies (contours, units: m/s) at 50°N during the ±15-day period relative to PULSE_lead (a) and PULSE_lag (b) CAOs; 50hPa geopotential height anomalies (shading, units: gpm) and zonal wind anomalies (contours, units: gpm) averaged over 15 to 8 days before peak dates of PULSE_lead (c) and PULSE_lag (d) CAOs

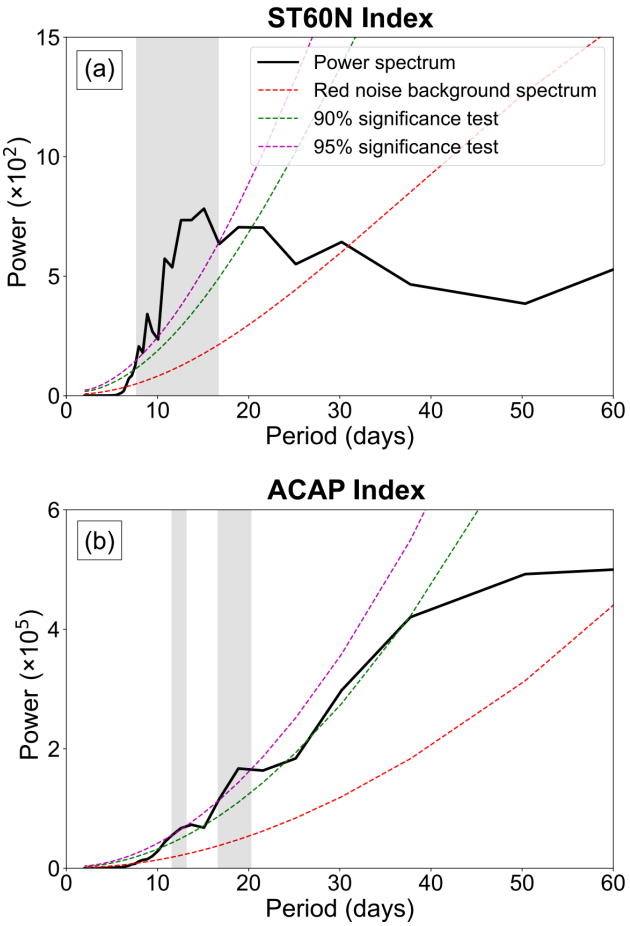

1011

1012 **Fig. 1** Fourier power spectra of (a) ST60N (units: 1) and (b) ACAP (units: %) index in winters

1013 (November – March) from 1979 to 2024.This period serves as the common analysis time frame for

1014 all subsequent figures

1015

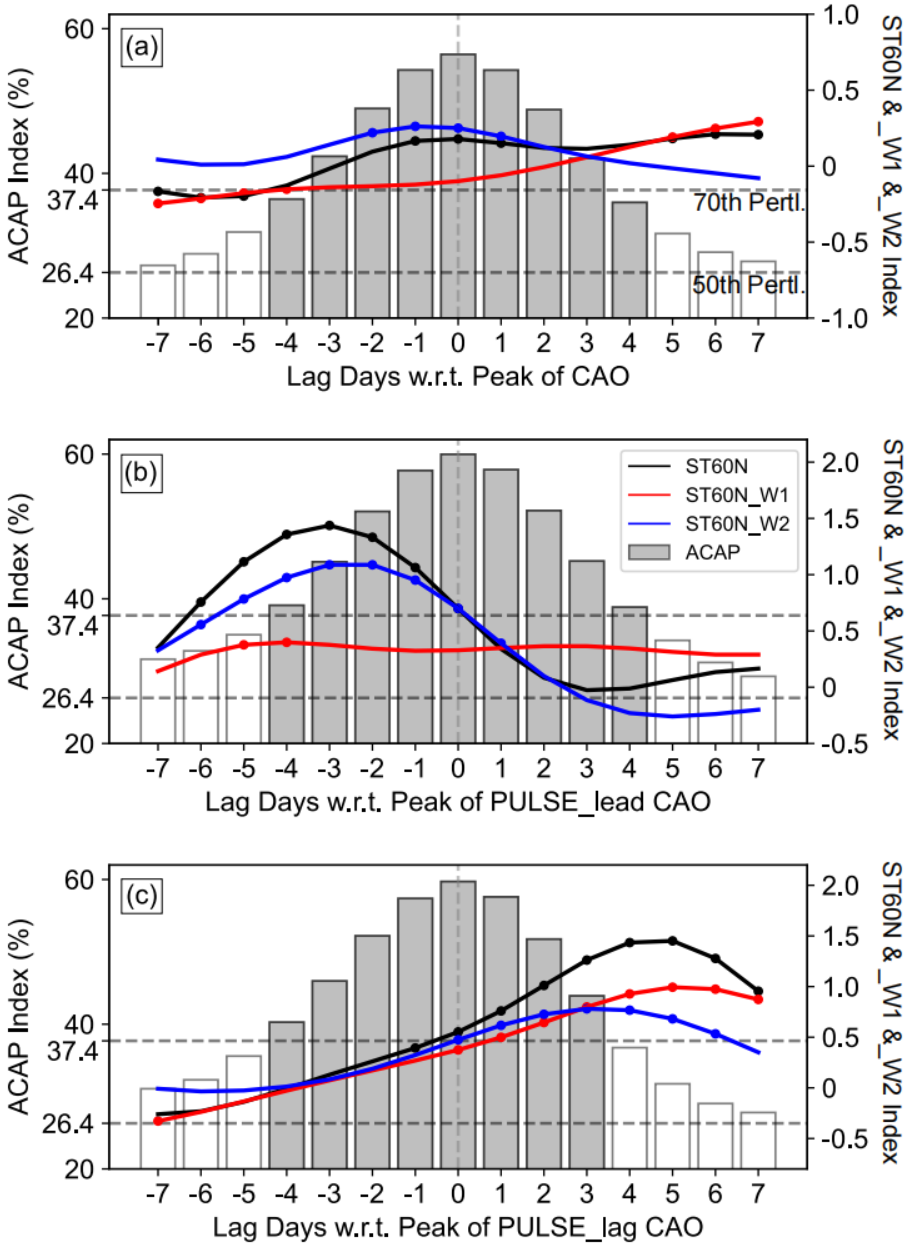

Fig. 2 Composite of the ACAP index (bars, units: %) and ST60N index and its wavenumber-1 and wavenumber-2 components (lines) during the ±7-day windows centered on peak dates of CAOs: (a) all events, (b) PULSE_lead type events, and (c) PULSE_lag type events. Dots and filled symbols denote statistical significance at the 95% confidence level. The 50th and 70th percentile of ACAP index are highlighted by the horizontal dashed line

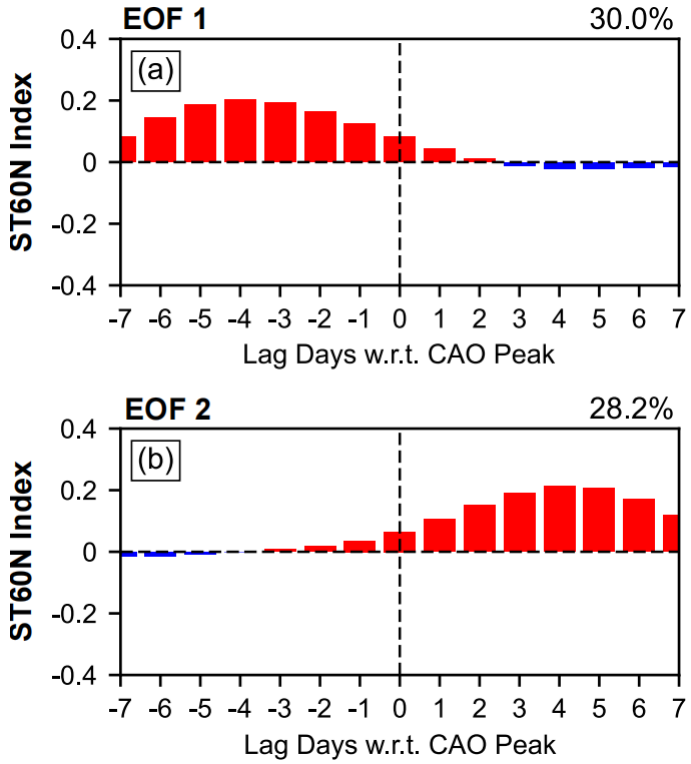

1023

1024 **Fig. 3** Dominant evolution patterns of ST60N, indicated by the spatial patterns of (a) the first and

1025 (b) the second EOF modes for the ST60N index during the ±7-day windows centered on peak dates

1026 of 173 Asian CAOs. The percentage of explained variance for each mode is labeled above respective

1027 panel

1028

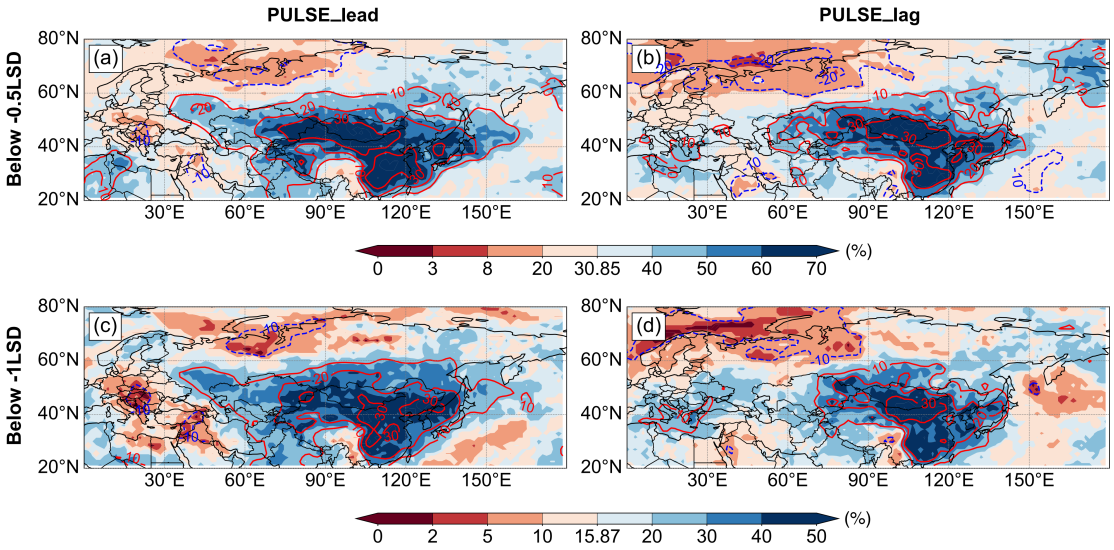

1029

1030 **Fig. 4** Spatial distribution of the occurrence probability (shading; units: %) of grid points with 2m
1031 temperature anomalies below -0.5 (a–b) and -1.0 (c–d) local standard deviation (LSD) thresholds
1032 during all days when the ACAP index exceeds its 50th percentile for CAO events belonging to
1033 “PULSE_lead” (a, c), “PULSE_lag” (b, d) types. Probability differences relative to all winter days
1034 are overlaid as contours

1035

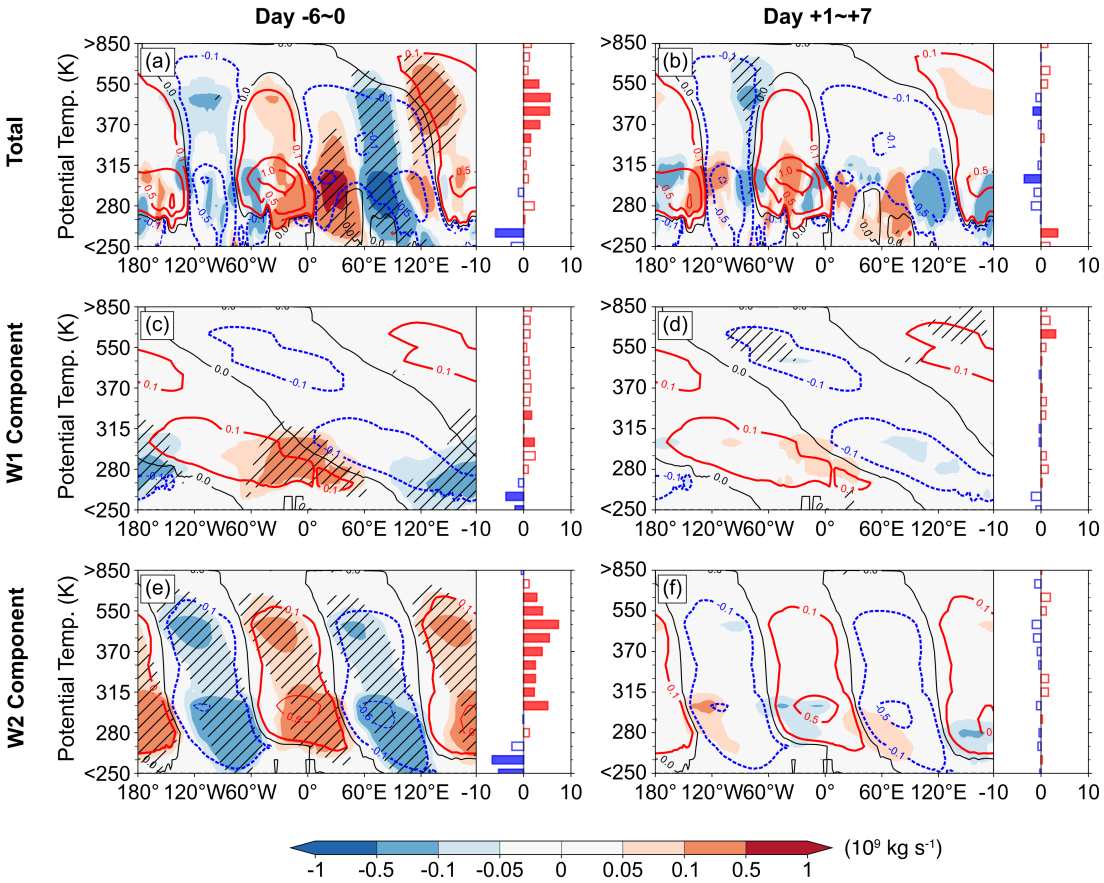

Fig. 5 Composite isentropic meridional mass flux anomalies at 60°N (shadings, 10^9 kg s^{-1}) averaged over days -6 to 0 (a, c, e) and days +1 to +7 (b, d, f) relative to peak dates of Asian CAO events belonging to PULSE_lead type: total (a–b), wavenumber-1 (c–d) and wavenumber-2 components (e–f). Contours depicts winter climatological mean and right panels display zonal integrated anomalies which above 330K was multiplied by 5 for visualization. Hatched area and colored bars are significant at 95% confidence level

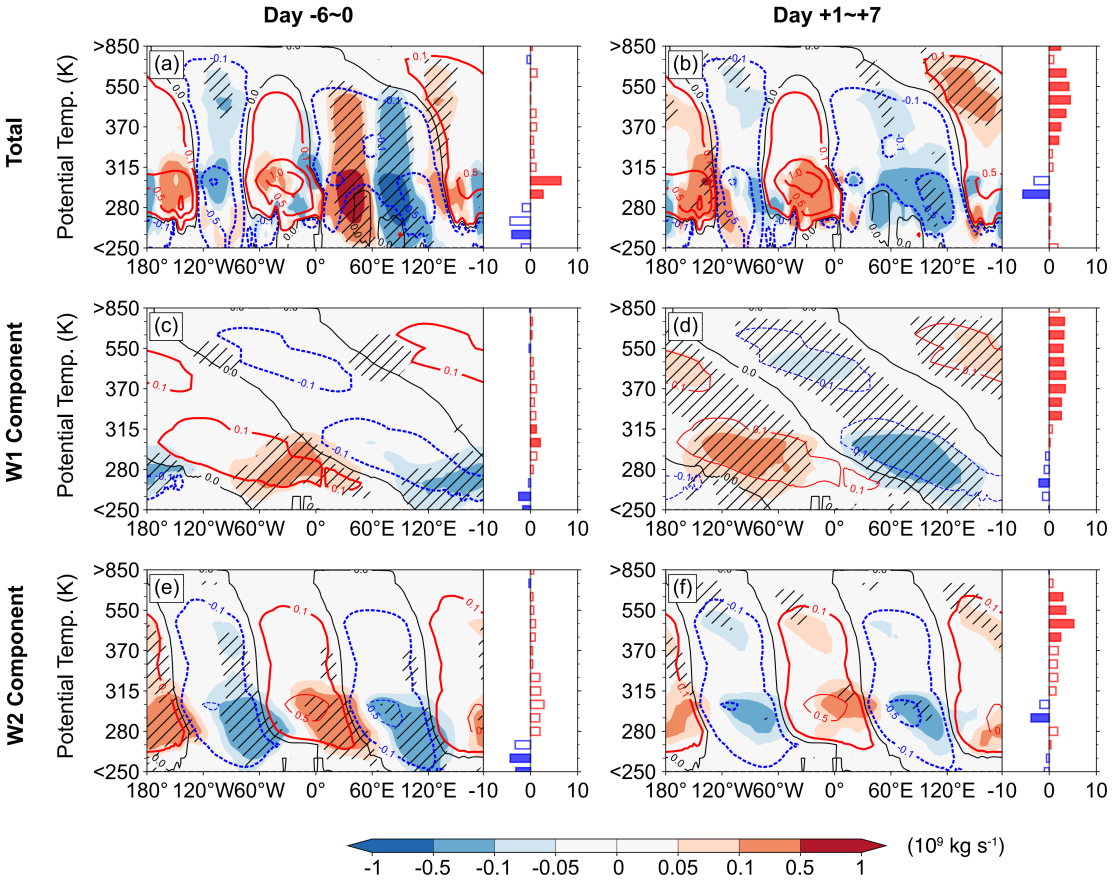

1044

1045 **Fig. 6** As in Figure 5, but for PULSE_lag type

1046

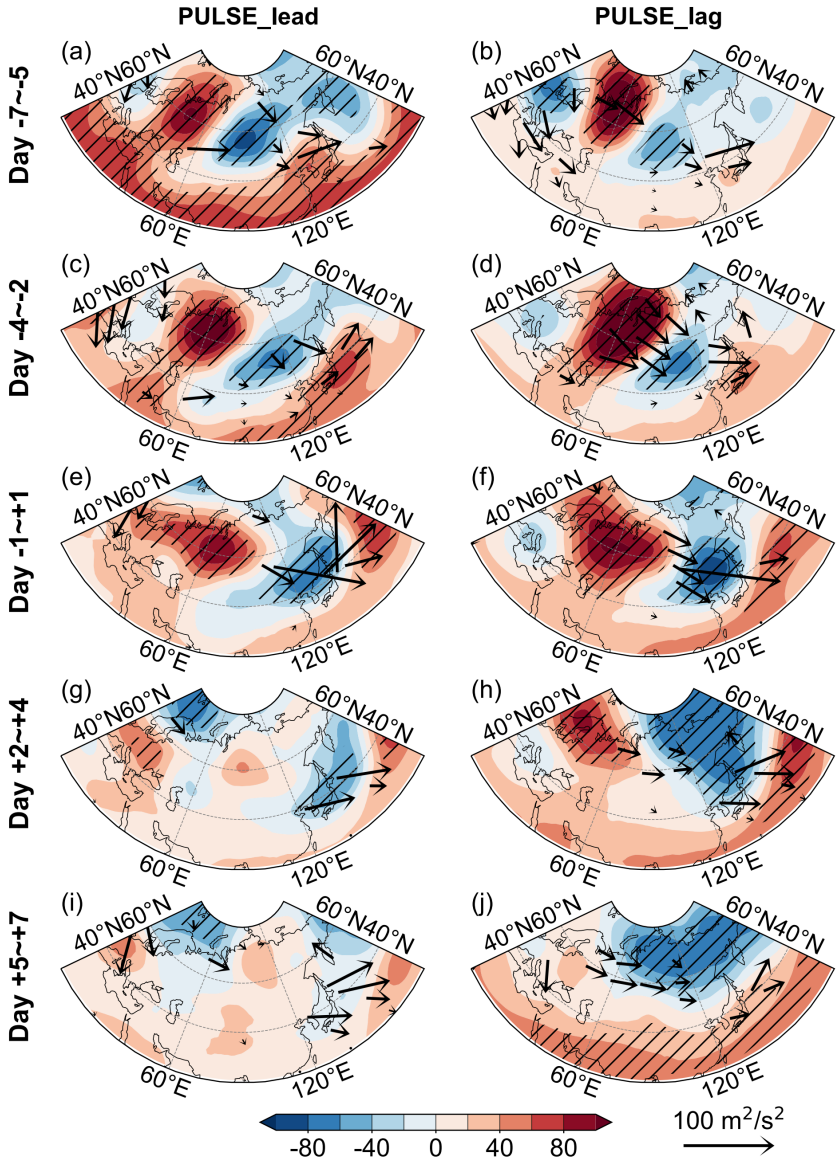

Fig. 7 Composite maps of 500 hPa geopotential height anomalies (shading, gpm) and horizontal wave activity flux (arrows, m^2/s^2) for PULSE-lead and PULSE-lag CAOs relative to their peak dates. Five temporal phases are analyzed: lead times of −7 to −5 days (a–b), −4 to −2 days (c–d), −1 to +1 days (e–f), lag times of +2 to +4 days (g–h), and +5 to +7 days (i–j). All arrows and hatched areas denote statistical significance at the 95% confidence level

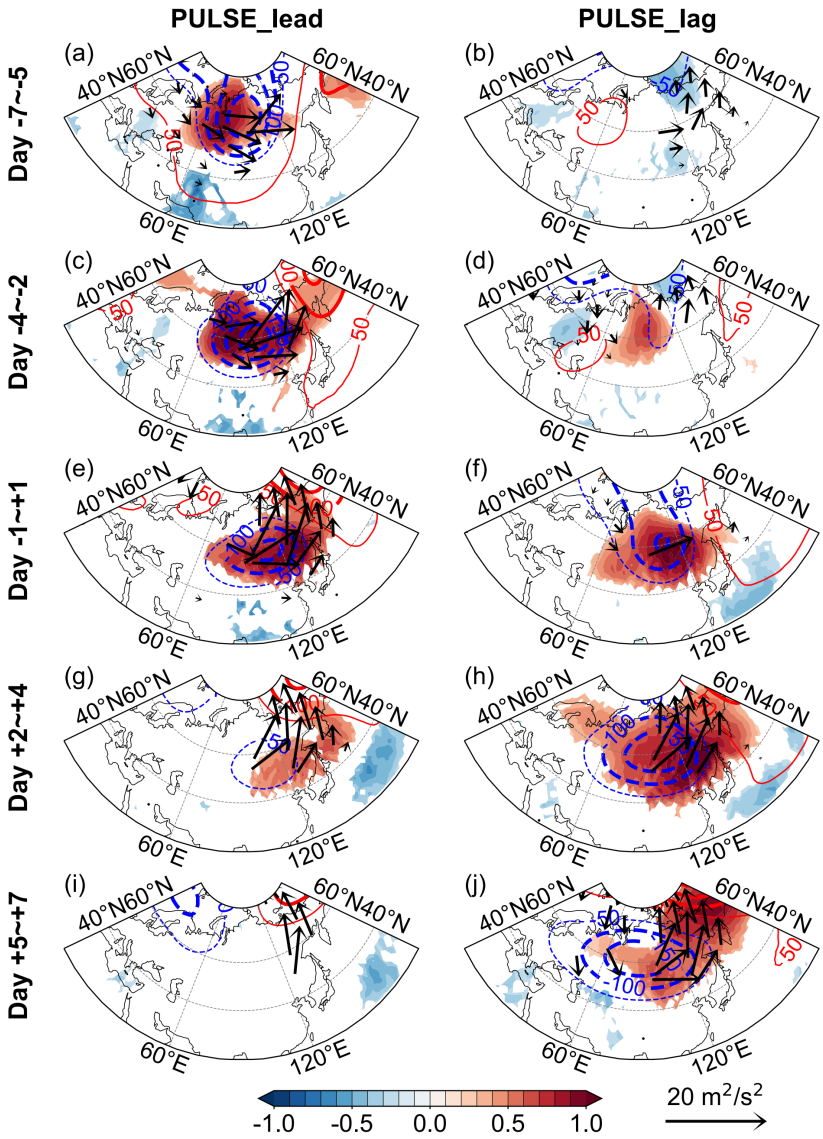

Fig. 8 Composite fields of 50 hPa geopotential height anomalies (contours, units: gpm), vertical wave activity flux anomalies at 100 hPa (shading, normalized by time), and horizontal wave activity flux at 100 hPa (arrows, units: m²/s²) for PULSE-lead and PULSE-lag CAOs: days −7 to −5 (a–b), days −4 to −2 (c–d), days −1 to +1 (e–f), days +2 to +4 (g–h), and days +5 to +7 (i–j) relative to peak dates. Bold contours indicate statistical significance at the 95% confidence level, and only significant wave fluxes are displayed

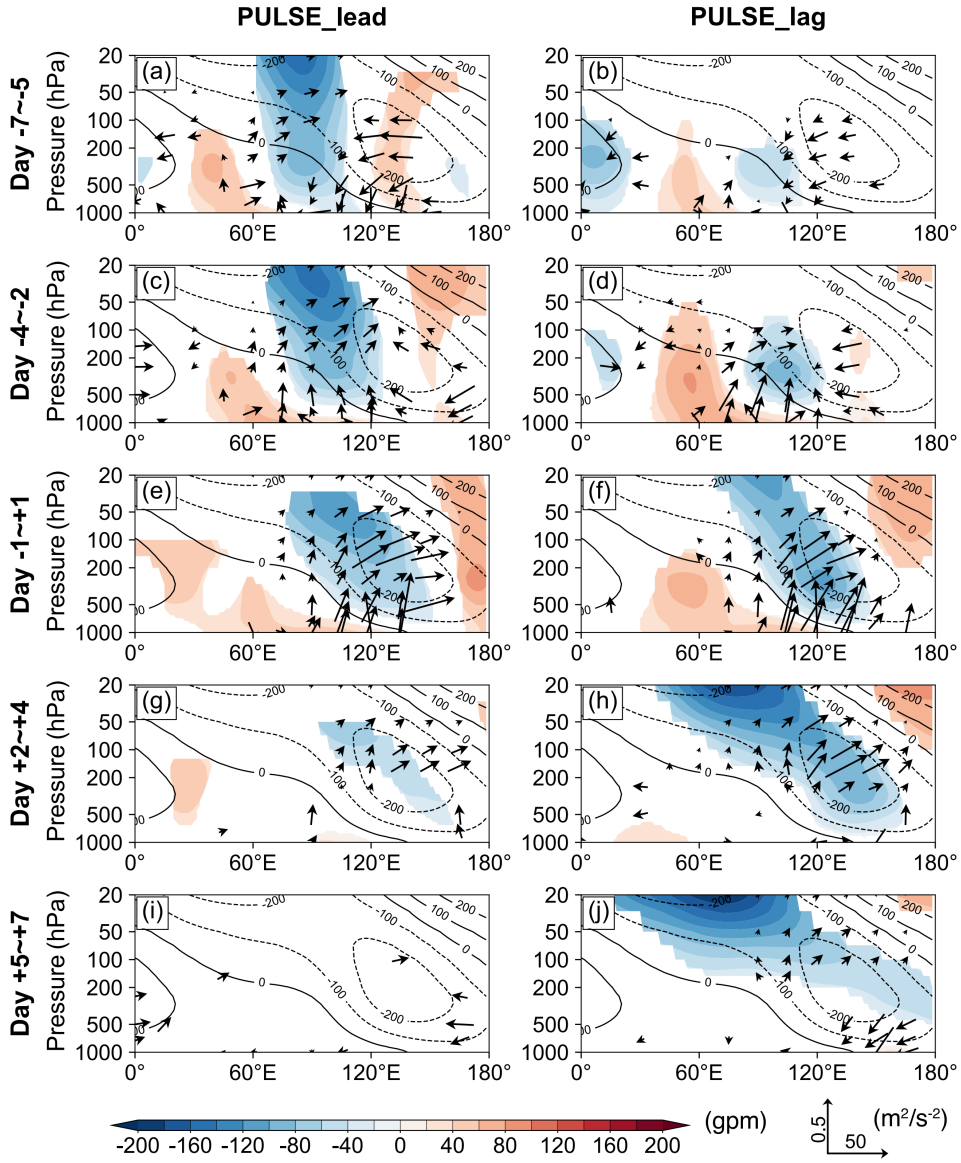

Fig. 9 Composite evolution of T-N flux anomaly vectors (zonal and vertical components; units: m^2/s^2) and geopotential height anomaly (shading; units: gpm) averaged over 45–65°N for five periods of (a) PULSE-lead and (b) PULSE-lag CAOs. The climatological winter mean geopotential height (contours; units: gpm) is overlaid. Only anomalies statistically significant at the 95% confidence level are displayed. The levels above 200 hPa is magnified by a factor of three for visualization

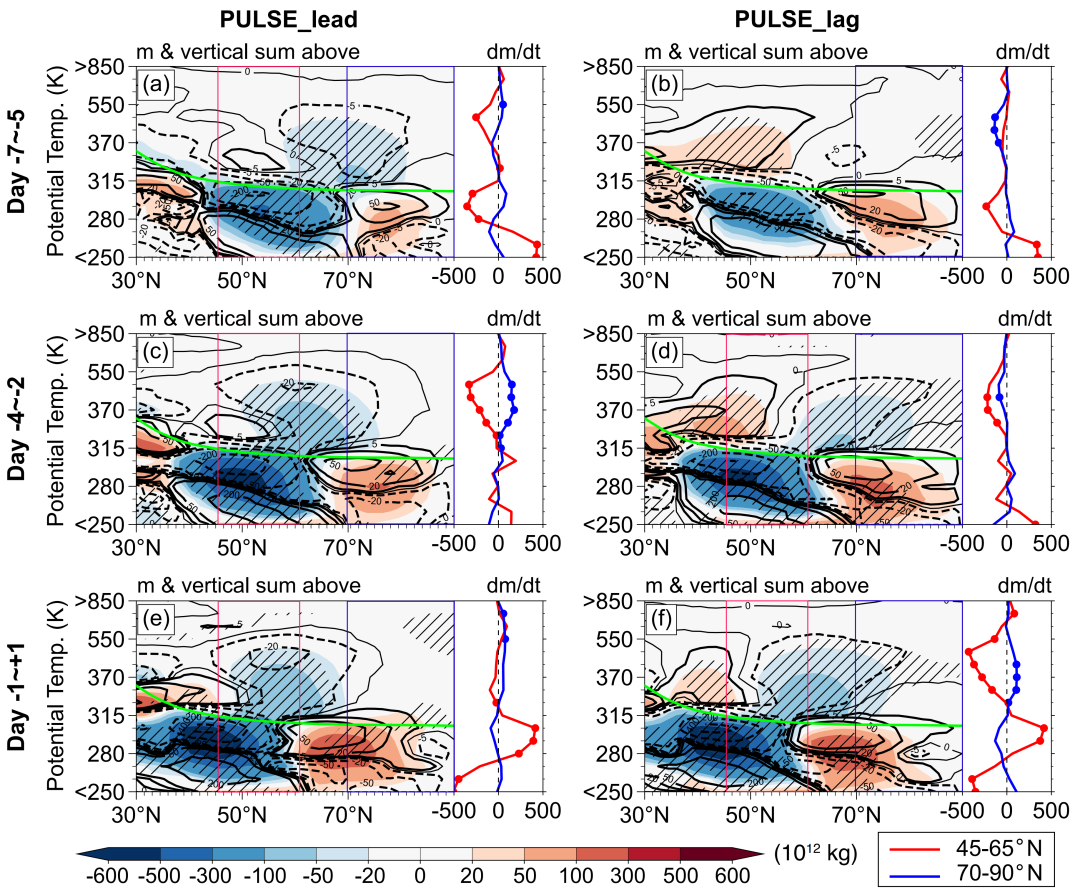

1070

1071 **Fig. 10** Zonal sum of isentropic mass anomalies (contours, units: 10^{12} kg) over the longitude band
1072 70–150°E and their vertically integral above each isentropic level (shading, units: 10^{12} kg) for
1073 PULSE-lead (left column) and PULSE-lag (right column) CAOs during three periods relative to the
1074 peak dates: days -7 to -5 (a, b), -4 to -2 (c, d), and -1 to +1 (e, f). The rightmost attached panels
1075 display the daily tendency of mass anomalies (units: 10^{12} kg; levels above 350K are amplified by
1076 5), summed over midlatitudes (45–65°N, red curve) and high latitudes (70–90°N, blue curve),
1077 respectively. Hatched area, thickened contours and dotted curves denote statistical significance at
1078 the 95% confidence level. The solid green line represents the climatological winter mean
1079 thermodynamic tropopause potential temperature
1080

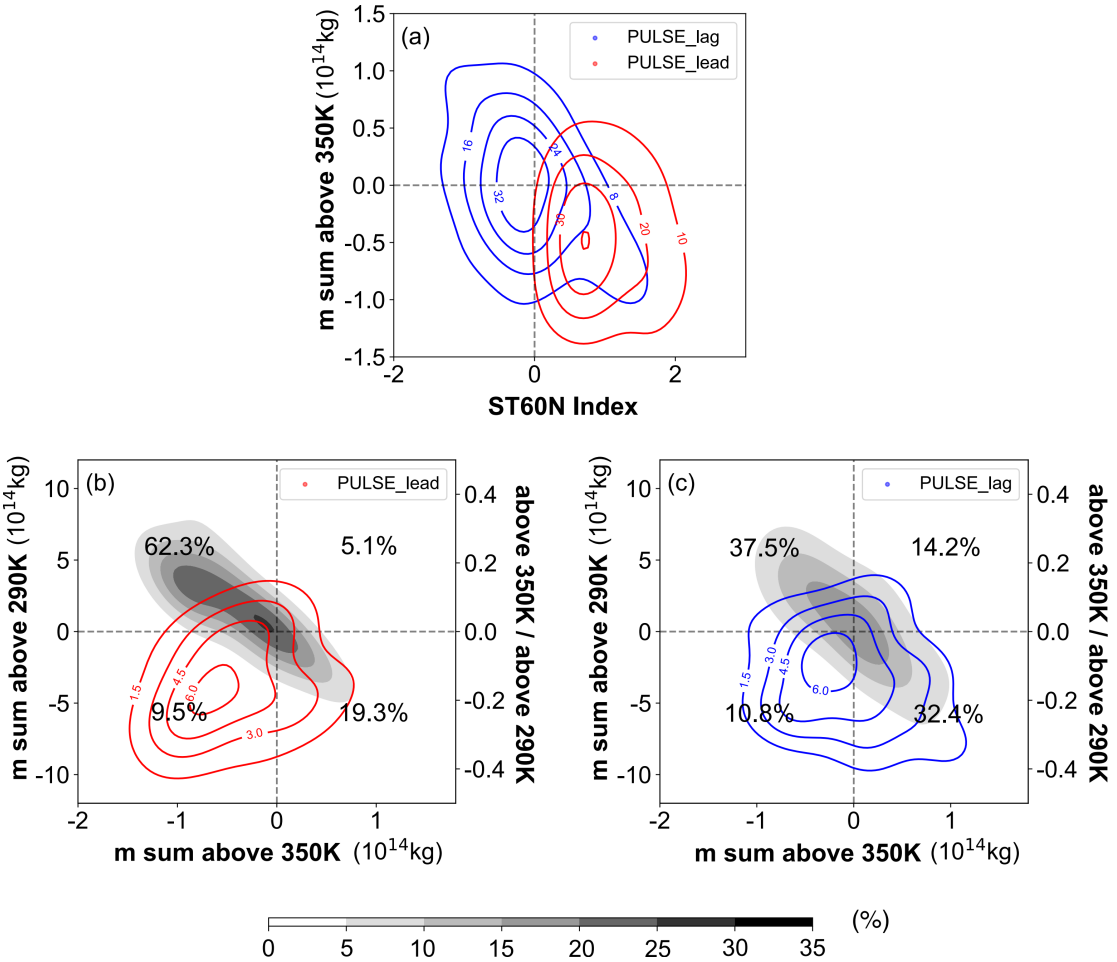

Fig. 11 Joint probability distributions (contours, %) of key dynamical and thermodynamical anomalies associated with CAO events. (a) ST60N during days -7 to -2 relative to peak dates versus regionally integrated isentropic mass anomalies above 350K in the low-pressure anomaly key region (45–65°N, 70–150°E; averaged over days -4 to +1). (b, c) Joint distributions of mass anomalies above 350 K versus (i) those above 290K (contours) and (ii) their ratio (350K/290K; shadings) for the same period (days -4 to +1 relative to peak dates of (b) PULSE_lead and (c) PULSE_lag events). Quadrants labels indicate the probability of samples falling within each bin of the 350 K mass anomaly versus the 350 K/290 K ratio

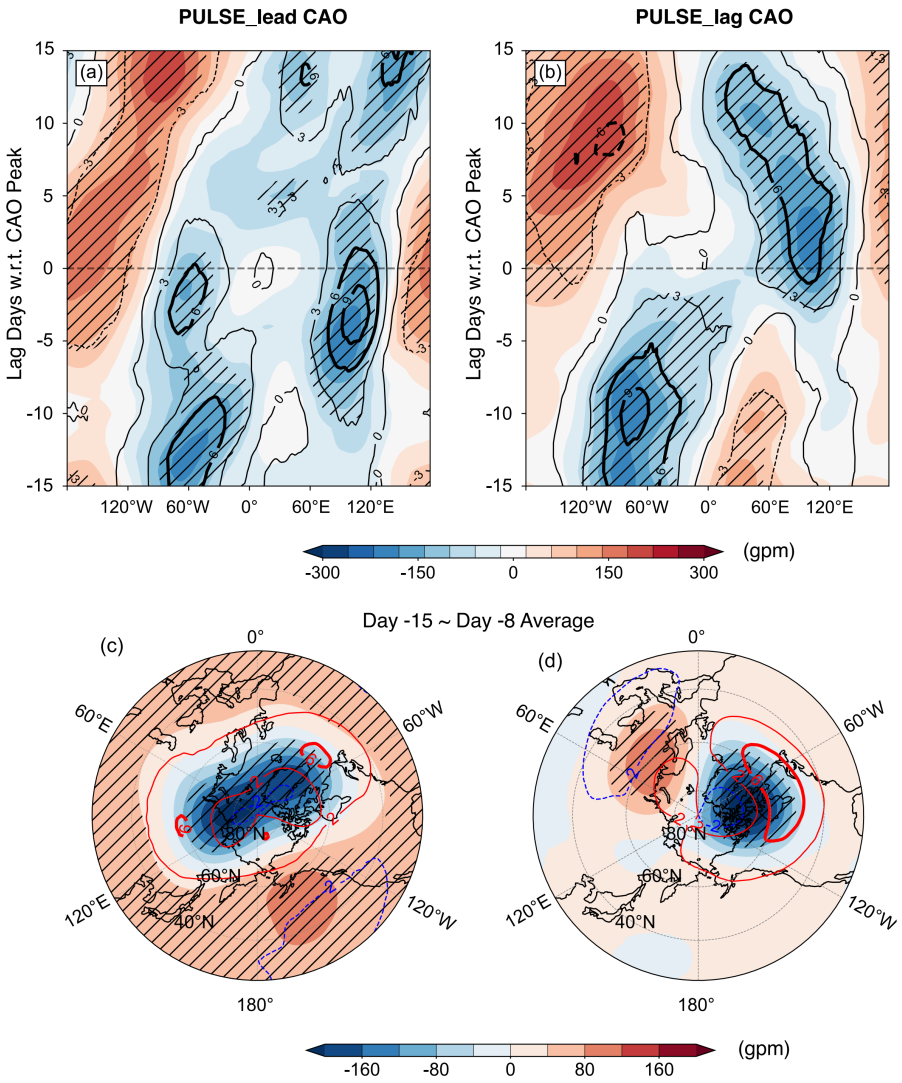

Fig. 12 Composite of (a, b) 50hPa geopotential height anomalies (shading, units: gpm) averaged over 50°N–80°N and zonal wind anomalies (contours, units: m/s) at 50°N during the ±15-day period relative to PULSE_lead (a) and PULSE_lag (b) CAOs; 50hPa geopotential height anomalies (shading, units: gpm) and zonal wind anomalies (contours, units: gpm) averaged over 15 to 8 days before peak dates of PULSE_lead (c) and PULSE_lag (d) CAOs